Trinity College Dublin
Coláiste na Tríonóide, Baile Átha Cliath
The University of Dublin

Investigation into the potential of embedded strain sensors for force measurement in grinding wheels

William Dempsey

Supervisor: Dr Garret O'Donnell

April 14, 2024

A Dissertation submitted in partial fulfilment
of the requirements for the Degree of
MAI (Mechanical and Manufacturing Engineering)

Declaration

I hereby declare that this Dissertation is entirely my own work and that it has not been submitted as an exercise for a degree at this or any other university.

I have read and I understand the plagiarism provisions in the General Regulations of the University Calendar for the current year, found at `http://www.tcd.ie/calendar`.

I have completed the Online Tutorial on avoiding plagiarism 'Ready Steady Write', located at `http://tcd-ie.libguides.com/plagiarism/ready-steady-write`.

I consent to the examiner retaining a copy of the thesis beyond the examining period, should they so wish (EU GDPR May 2018).

I agree that this thesis will not be publicly available, but will be available to TCD staff and students in the University's open access institutional repository on the Trinity domain only, subject to Irish Copyright Legislation and Trinity College Library conditions of use and acknowledgement.

Signed: William Dempsey Date: 14/04/24

Abstract

The global manufacturing industry is undergoing a fourth industrial revolution, in that its capabilities are greatly increasing due to technological advances. A notable recent development here is the introduction of smart tooling into machining processes, where sensors are used to monitor different types of physical quantities that are indicative of a tool's working states or the tool-workpiece interactions. The ideal smart tooling solution can be embedded directly in-situ i.e. directly onto the tool, and sensors which measure strain resulting from the forces acting on the tool show promise for this application.

Smart tooling is underdeveloped in the area of grinding, a process which involves an abrasive wheel rotating at high speeds to remove material from a workpiece. Grinding machine operators typically err towards conservative machining parameter choices to avoid issues such as workpiece damage, thereby leading to process inefficiencies. The information gained from an effective grinding tool monitoring system could allow for more calculated, and more aggressive, process parameter adjustments, thereby making grinding more precise and economical. Emerging strain sensing technologies, such as Surface Acoustic Wave (SAW) and Magnetostrictive (MR) sensors, show promise for grinding force measurement via integration into grinding wheels. A combined experimental and Finite Element (FE) modelling approach was used in this project to evaluate the sensor potential for this application. The grinding wheel geometry was simplified and a static loading scenario assumed to facilitate this approach.

The bending strain resulting from out-of-plane (i.e. axial) grinding forces was found to occur at levels which were detectable by SAW and MR sensors. This eclipsed the shear strain resulting from in-plane (i.e. tangential or normal) grinding forces, which makes the in-plane forces difficult to detect. A number of modified grinding wheel designs were evaluated, including thinned and slotted geometries. These designs exhibited a more pronounced strain response than the conventional grinding wheel design, although they too demonstrated a far greater propensity to exhibit bending strain than shear strain.

It was thus concluded that embedded strain sensors have strong potential for measuring out-of plane grinding forces, but limited potential for measuring in-plane forces. SAW sensors emerge as the optimal choice for this application, although MR sensors also demonstrate some potential. Finally, it was proposed that future work should investigate the grinding wheel shaft as a potential embedded sensor location for the measurement of tangential and normal grinding forces.

Lay Abstract

The global manufacturing industry is currently undergoing a fourth industrial revolution, in that its capabilities are greatly increasing due to technological advances. A notable recent development here is the use of smart tooling in machining processes (processes which remove material from a workpiece with cutting tools to form a finished component). Smart tooling provides information about tools as they are being used in manufacturing, and the ideal smart tooling solution can be embedded directly onto the tool.

Smart tooling is underdeveloped in the area of grinding, a process which involves an abrasive wheel rotating at high speeds to remove material from a workpiece. Grinding machine operators typically choose to incorporate significant margins of error when managing grinding processes, thereby leading to process inefficiencies. The information gained from an effective grinding tool monitoring system could allow for allow for more calculated, and more aggressive, process management decisions, thereby making grinding more precise and economical.

Innovative sensor technologies show promise for force measurement in grinding processes, with strain (deformation) sensors standing out among these potential solutions. Surface Acoustic Wave (SAW), and Magnetostrictive (MR) sensors are the most promising of these strain sensing technologies. This project looked to evaluate if embedded strain sensors could be used for force measurement in grinding wheels during operation, and if this would allow the forces acting on the wheel to be calculated.

Computer models of grinding wheels were created to predict the strain in them under applied forces, and experiments were conducted to check the validity of the predictions. A number of grinding wheel designs were evaluated with the computer model, using the strain predictions to assess whether they could facilitate grinding force measurement. A conventional grinding wheel design was assessed first, with a number of modified designs being evaluated after this.

It was thus concluded that embedded strain sensors demonstrated significant potential for the measurement of forces acting in certain directions, but forces acting in others may be difficult to detect. The modified grinding wheel designs were predicted to enhance the force measurement capabilities of embedded strain sensors, but the modifications may cause the grinding wheel to bend during operation. Finally, it was proposed that future work should investigate the grinding wheel shaft as a potential sensor location to allow the measurement of grinding forces in all directions.

Acknowledgements

Many people have offered their assistance, support, and guidance throughout the course of this project, for which I am very grateful.

Firstly, I would like to thank my supervisor, Dr Garret O'Donnell, for his time and guidance which were of huge benefit to me throughout the project.

A special thanks to Dr Natalia Lishchenko for her support and insights which were instrumental to my completion of the project.

I would also like to thank the technical staff of the Department of Mechanical and Manufacturing Engineering, especially to Rob Dunbar for his many useful suggestions and endless patience.

Finally, thank you to my parents, Anne and John, for their constant and immense support and encouragement throughout my academic career.

Contents

1 Introduction **1**

1.1 Research Background . . . 1

1.2 Research Problem . . . 2

1.3 Research Objectives . . . 4

1.4 Project Approach . . . 5

2 Background and Literature Review **6**

2.1 Smart Tooling . . . 6

2.2 Grinding Background and Monitoring . . . 8

2.2.1 Grinding Forces . . . 10

2.3 Strain Theory and Measurement . . . 12

2.3.1 Traditional Strain Sensing Technologies . . . 13

2.3.2 Novel Strain Sensing Technologies . . . 16

2.4 Grinding Wheel Analysis Using In-Plane Torsion Testing . . . 18

2.5 Strain Modelling and Validation . . . 20

2.6 Summary . . . 21

3 Simplified Disc Structure: Experimental Approach **22**

3.1 Simplifications To Grinding Setup . . . 22

3.2 Strain Measurement . . . 23

3.2.1 Strain Gauge Application . . . 23

3.2.2 Data Collection . . . 24

3.3 Torsion Testing . . . 25

3.3.1 Grinding Wheel and Discs . . . 25

3.3.2 Test Rig . . . 25

3.3.3 Static Loading Procedure . . . 26

3.4 Finite Element Model . . . 26

3.4.1 Geometry and Properties . . . 27

3.4.2 Mesh . . . 28

3.4.3 Boundary Conditions . . . 29

3.4.4 Strain Gauges . . . 30

3.4.5 Simulation Output . . . 30

3.5 Summary . . . 31

4 Simplified Disc Structure: Results and Discussion **32**

4.1 5 mm Disc Tests . . . 32

4.1.1 Approach . . . 32
4.1.2 Results . . . 33
4.2 3 mm Disc Tests . . . 34
4.2.1 Approach . . . 34
4.2.2 Results . . . 35
4.3 FE Model Validation . . . 35
4.3.1 Approach . . . 35
4.3.2 Results . . . 36
4.4 Summary . . . 38

5 Simplified Beam Structure **39**
5.1 Disc to Beam Simplification . . . 39
5.2 Refined Strain Gauge Application Process . . . 40
5.3 Bending Strain Investigation . . . 41
5.3.1 Approach . . . 41
5.3.2 Results . . . 43
5.4 Shear Strain Experiment . . . 45
5.4.1 Approach . . . 45
5.4.2 Results . . . 45
5.5 Beam Deflection Investigation . . . 46
5.5.1 Approach . . . 46
5.5.2 Results . . . 47
5.6 Summary . . . 48

6 Sensor Potential Evaluation **50**
6.1 FE Modelling Approach . . . 50
6.2 Results and Discussion . . . 53
6.2.1 Axial Loading . . . 53
6.2.2 Tangential Loading . . . 54
6.2.3 Normal Loading . . . 54
6.3 Force Response Comparison . . . 55
6.3.1 Embedded Sensor Potential: Conventional Grinding Wheel . . . 56
6.3.2 Embedded Sensor Potential: Optimised Designs . . . 57
6.4 Summary . . . 57

7 Conclusion **58**

A1 Experimental Setups **73**
A1.1 Coordinate System Definition . . . 73
A1.2 Experimental Coordinates . . . 74

A2 Additional FE Model Information **76**
A2.1 Material Properties 76
A2.2 Chapter 6 Meshing 76
A2.3 Chapter 6 Setup 78

List of Figures

1.1 Grinding wheel with worn abrasive layer. 2
1.2 Combined experimental/FE modelling approach. 5

2.1 The use of cutting power for grinding process characterisation 8
2.2 Flat surface grinding, cylindrical surface grinding, and toroidal grinding wheel 9
2.3 Grinding force components 10
2.4 Strain gauges installed on grinding workpiece platform 11
2.5 Quarter bridge circuit for strain measurement 15
2.6 The three basic types of rosette strain gauge 16
2.7 Twin bridge and grooved disc setups for in-plane torsion testing 19

3.1 Schematic diagrams of a grinding wheel in motion, a disc under torsion, and a disc segment under torsion 23
3.2 Grinding wheel cross-section 25
3.3 Use of custom components in torsion testing setup 26
3.4 Finite element mesh for 3 mm disc model 28
3.5 Mesh convergence comparison and independence analysis 29
3.6 Finite element model boundary conditions 29
3.7 Equivalent strain plot generated with construction path feature 31

4.1 In-plane torsion testing of 5 mm disc 32
4.2 Signal from strain gauge installed on 5 mm disc (after applying 30 point averaging) 33
4.3 In-plane torsion testing on 3 mm disc 34
4.4 Strain Gauge 1 signal (after 30 point averaging) 35
4.5 Strain gauge and clamp position labelling 36
4.6 Strain Gauge 1 results 37
4.7 Comparison of Strain Gauge 1 results at 30 Nm torque to FE model 37

5.1 Schematic diagram and practical application of the disc to beam simplification 40
5.2 Experimental setup for bending strain tests 42
5.3 FE beam model mesh 42
5.4 Kistler sensor bending strain measurements 43
5.5 Strain Gauge 2 and Strain Gauge 3 bending strain measurements 44
5.6 Shear strain values recorded by the 5 strain gauges 46
5.7 Digital dial indicator for detecting out-of-plane beam deflection 47
5.8 Out-of-plane beam deflection under shear loading 48

6.1 Conventional grinding wheel and optimised designs for enhanced strain sensitivity 51
6.2 Boundary conditions for axial, normal, and tangential loading simulations . . 52
6.3 Wheel region labelling and equivalent strain plot for bridges design 52
6.4 Bending strain distributions under applied axial force 53
6.5 Shear strain distributions under applied tangential force 54
6.6 Shear strain distributions under applied normal force 55
6.7 Strain distributions in conventional grinding wheel 56

A1.1 Disc coordinate system 73
A1.2 Strain gauge and clamp angle definitions 74

A2.1 Grinding wheel mesh. 76
A2.2 Thinned grinding wheel mesh. 77
A2.3 Slotted disc mesh. 77
A2.4 Bridge disc mesh. 77

List of Tables

2.1 Peak grinding forces reported in the literature 10

3.1 Finite element model mesh parameters 28

5.1 Primary strain direction calculated from experimental results 44
5.2 Maximum out-of-plane deflections and corresponding bending strains 48

6.1 Comparison of average strains across Region B 55

A1.1 Coordinates for 5 mm disc experimental setup 74
A1.2 Coordinates for first 3 mm disc experiment 74
A1.3 Coordinates for second 3 mm disc experiment 75
A1.4 Coordinates for beam experiments 75

A2.1 Material properties as per ANSYS Mechanical Library. 76
A2.2 Construction path coordinates for grinding wheel simulations. 78

Nomenclature

A	Area	m^2
F	Force	N
F_a	Axial force	N
F_n	Normal force	N
F_t	Tangential force	N
E	Modulus of Elasticity/ Young's Modulus	Pa
I	2nd Moment of Area	mm^4
L	Length	m
T	Torque	Nm
t	Thickness	m
α	Angle about the X-axis	$^\circ$
β	Angle between clamp and sensor positions	$^\circ$
ϵ	Strain	m/m
σ	Stress	Pa
AWG	American Wire Grade	
CBN	Cubic Boron Nitride	
CNC	Computer Numerical Control	
FBG	Fiber Bragg Grating	
FE	Finite Element	
HEDG	High Efficiency Deep Grinding	
MEMS	Micro Electro-Mechanical Systems	
MR	Magnetostrictive	
SAW	Surface Acoustic Wave	
SG	Strain Gauge	

1 Introduction

1.1 Research Background

Various machining operations are typically involved in the manufacture of complex precision parts, such as aerospace and bioengineering components. Processes such as milling, drilling, grinding, and turning use cutting tools to remove material from a workpiece and create the finished component. Contemporary manufacturing processes leverage computer numerically controlled (CNC) machines (also referred to as machine tools) to guide the motion of the cutting tool, achieving high levels of precision in machining.

Recent academic literature indicates that the global manufacturing industry is undergoing a fourth industrial revolution, in that its capabilities are greatly increasing due to technological advances. This paradigm shift is often referred to as "Industry 4.0" or "Smart Manufacturing" and is characterised by elements such as greatly enhanced manufacturing flexibility, automation, component intelligence and integration [1]. In the machining domain, advances have included the implementation of novel sensors, sensor systems and sensing methodologies to measure workpieces and tools [2].

There has also been an emergence of smart tooling in recent years. Smart tooling is the use of "sensors to monitor different types of physical quantities that are indicative of a tool's working states or the tool-workpiece interactions" [3]. The ideal smart tooling solution can be embedded in-situ i.e. directly onto the tool [4], [5]. Placing the sensor in close proximity to its target (i.e. close to the cutting zone) enhances the quality of the sensor signal and enables more effective real-time monitoring. Embedding the sensors increases visibility of the machining process, allowing early identification of issues such as tool wear, tool breakage or machine malfunction, thereby reducing equipment downtime [6]. Passive sensors, which operate without an external power source [7], are particularly desirable for this purpose as they eliminate the need for cumbersome battery packs or power cables.

1.2 Research Problem

One field where smart tooling is lacking is the area of grinding- a process which involves a wheel rotating at high speeds to remove material from a workpiece. Grinding is the preferred machining method for finishing in many industrial applications, as it provides a high-quality surface finish. However, there are a number of challenges in modern grinding processes. Some of the key issues include ensuring workpiece surface integrity, upholding process reliability and reducing energy wastage [8]. Phenomena such as chatter (self-excited wheel vibration) and grinding burn (localised overheating of the workpiece) are also prevalent in modern grinding processes, leading to dimensional inaccuracies and residual stresses in workpieces [9], [10], [11]. Each of these issues can be very costly to the manufacturer, but solutions may be possible through the use of smart tooling systems.

One smart tooling solution with significant potential for grinding process improvements would be the use of force monitoring systems, the requirement for which as illustrated in Figure 1.1. Here, the lack of a suitable method for measuring grinding forces resulted in excessive force being unknowingly applied to the grinding wheel during contact with the workpiece. This led to a wearing away of the abrasive material on the grinding wheel periphery and created stress concentrations in the workpiece surface. The workpiece was no longer fit for purpose, and the abrasive material had to be redressed- a process where the grinding wheel surface is cut to expose fresh abrasive grains and which can be very costly for the manufacturer.

(a) Isometric view. (b) Zoomed in side view.

Figure 1.1: Grinding wheel with worn abrasive layer.

Grinding machine operators tend to err towards conservative choices of machining parameters in order to avoid such occurrences, thereby leading to grinding process inefficiencies [12]. An effective force monitoring solution could help with this problem by providing machine operators with valuable information. Better knowledge of the system's state and behaviour would enable calculated process parameter adjustments which move away from the ultra-conservative approach, thereby making the process more economical.

The problem constitutes a significant research opportunity whose solution could be extremely valuable, particularly in sectors requiring precise tolerances. Grinding processes are already widely used in the aerospace industry for the manufacture of high-quality components such as high-pressure turbine blades [9] and further productivity improvements here would prove extremely advantageous. A force monitoring solution would be similarly beneficial in the field of biomedical engineering, where orthopaedic implants such as hip and knee replacements have demanding surface finish requirements [13]. Current smart tooling solutions are unsuited to this application, as they involve the use of customised cutting tools, and most manufacturers are unwilling to replace the tools already used and validated in their processes. An additional issue here is the common requirement for batteries or charging circuits for powering the smart tooling solutions, which add complexity to already complex processes.

Embedded passive strain sensors emerge as a possible approach for monitoring grinding forces These sensors are compact, lightweight, and have potential for integration directly onto the grinding wheel structure. Embedded sensors have not been used to monitor grinding forces thus far, as existing attempts have focused mostly on sensors positioned on the workpiece platform [14], [15] or head stock and tail stock [16], [17], [18], (depending on the category of grinding machine being monitored). These sensors tend to be removed from the wheel-workpiece contact area and, as a result, may fail to capture important process information. Herzenstiel et al. [19] note that a precise observation of the grinding process calls for a measuring technique as close as possible to the contact zone.

Surface Acoustic Wave (SAW) and Magneto-Resistive (MR) strain sensors currently stand as the most promising technologies for embedded sensing applications. These novel sensors have already exhibited force measurement [20], [21] and passive operation potential [22], [23] in previous studies so they may represent an appropriate solution. However, further research is required before these sensors can be implemented on grinding wheels. Application of SAW and MR sensors is costly and time-consuming, so the work to investigate the issue must be completed before they can be deployed. Particularly important here is the requirement to evaluate the potential of strain sensors for force measurement in grinding wheels. It is not currently known if the strain behaviour of a grinding wheel can be used to infer details about the forces acting on it. For the sensors to bear potential for force measurement, the wheel must exhibit strain in response to applied forces, in a manner which is both measurable and predictable. This matter has not yet been discussed in the literature, so the project will focus on addressing it.

1.3 Research Objectives

The main project objective was to evaluate the potential of embedded strain sensors for force measurement in grinding wheels. To achieve this, it sought to address the issue of whether a grinding wheel exhibits strain in response to applied forces, and whether the level of strain occurring in the wheel is high enough that it can be measured by embedded strain sensors. The strain should also exhibit predictable strain patterns which have a consistent relationship with the torque and forces applied to the wheel. The former would allow strain measurements in the grinding wheel, with the latter allowing force values to be inferred from these measurements.

A combined experimental and FE modelling approach was used to investigate the strain behaviour of grinding wheels, facilitating an evaluation of embedded sensor potential. The project objectives were stated as:

1. To develop a finite element computer model of forces and torsion being applied to a grinding wheel. The applied loads should mirror those typically observed in real grinding processes;
2. To predict the strain exhibited by the wheel under these loading conditions;
3. To experimentally validate the finite element model with static loading tests analogous to grinding operating conditions; and
4. To use the obtained results to determine if embedded strain sensors can be used for force measurement in grinding wheels.

The area of strain in grinding wheels is not one which is addressed in the literature, so the project focused on providing a first level of understanding here through a combination of modelling and experimental work. It is expected that a more detailed analysis of the most optimum solution from the initial phase would take place in subsequent MAI projects.

The project scope solely encapsulated an evaluation of the potential of embedded strain sensors for force measurement to gain some fundamental insights into the sensitivities related to real world challenges in sensor application. As such, application of novel strain sensing technology to a grinding wheel was outside the project scope.

Finally, the potential of all strain sensors is being evaluated here (not just one specific type), so the project should prioritise the identification of strain behaviours on a macro level where necessary i.e. identifying general strain patterns rather than achieving absolute precision in results[1].

[1]Because of this, a systematic error evaluation will not be conducted here- error will be only evaluated where it is judged to be significantly affecting the results. This represents a deviation from common scientific practice, but it is a measure which allows the flexibility required to successfully fulfil the project's broad scope.

1.4 Project Approach

Finite Element (FE) simulations was used in this project to make predictions about the strain behaviour of grinding wheels, which could then be analysed to evaluate the embedded sensor potential for this application. A finite element model of a grinding wheel (or objects of comparable geometry) was created and subjected to the torsional moments and reaction forces that are typical of grinding processes. This then facilitated predictions about the wheel strain behaviour under applied loading.

The FE model should be validated before it can be used to provide insights about strain in grinding wheels. Reference measurements should be taken from grinding processes, or analogous systems, with which the FE model accuracy can be confirmed. Many examples were observed in the literature of the use of strain gauges for FE model validation [24], [25], [26], [27], and this approach will be adopted here.

As current technology cannot provide reference strain measurements on a moving grinding wheel, the experimental approach will involve strain measurement in systems analogous to grinding systems. Here, static loading tests will be used as a practical alternative to direct measurements of the grinding process, with the grinding conditions simplified to resemble a body in equilibrium[2]. Static loads will be applied to replicate the wheel loads experienced during operation,thereby providing an opportunity to capture reference measurements. This was expected to be an iterative process, with multiple revisions required to achieve FE model validation (as outlined in Figure 1.2).

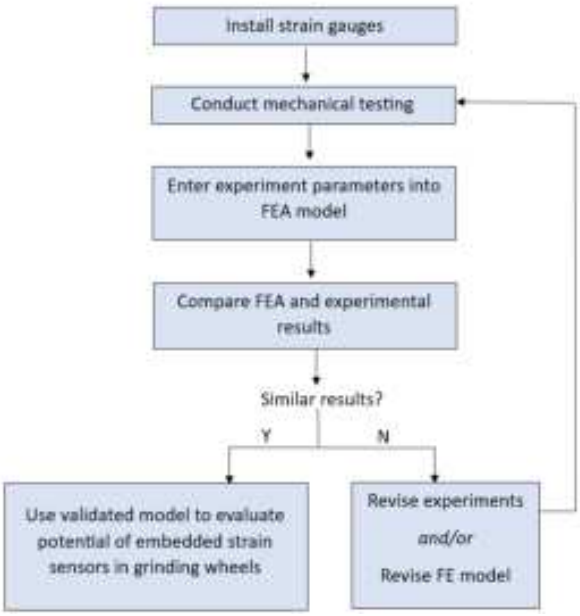

Figure 1.2: Combined experimental/FE modelling approach.

[2]Constant speed, torque, and cutting force generation during operation are assumed here.

2 Background and Literature Review

2.1 Smart Tooling

Cao et al. [3] defined smart tooling as the use of "sensors to monitor various types of physical quantities that are indicative of a tool's working states or the tool-workpiece interactions". Many recent developments in the manufacturing industry have been due to the implementation of novel sensors, sensor systems and sensing methodologies [2]. Smart tooling components are widely accepted to be somewhat independent, with characteristic features such as intelligence, service integration and data-driven models [28], [29].

Sensor systems have evolved from simple mechanical measuring tools to electrical sensors, and then to today's smart sensors and intelligent tooling systems [30]. Modern manufacturing systems can now connect numerous industrial processes within a single facility [31] and the sensors can be combined with local data processing systems and the Internet of Things (IoT) platform so decision making algorithms may be applied to their data in situ [32].

The area has been extensively researched, with many keynote papers detailing the state of the art in smart tooling and related topics. Papers from Tlusty and Andrews [33], Byrne et al. [34], Santochi and Dini [35], and O'Donnell et al. [36] have each provided updates on the status of smart tooling at different times over the last few decades. The work of Teti et al. [5] documented more recent progress, as did that of Bleicher et al. [37]. Each of these works agree on the importance of smart tooling using sensors to obtain real time data for manufacturing processes, so that informed decisions can be made for process improvement.

The potential enhancements that smart tooling can bring to manufacturing processes are extensive and varied. These improvements encompass enhanced system reliability and quality [38] and the enabling of advanced predictive maintenance [39], [40], and more flexible business models. Each measure can aid the manufacturing process optimisation and improve production profitability.

Lightweight and compact sensors are preferable for smart tooling systems [31], with wireless technology also being advantageous. They should also be robust enough to withstand the harsh environments typical of industrial settings [37]. The ideal smart component can be embedded directly into the tool but should not require the lengthy setup times and/or tool structure modifications that are characteristic of many academic tooling solutions [5].

Existing smart tooling literature mostly covers the in-process monitoring of 5 key

measurands- acoustic emission (AE), temperature, vibration, motor power/current and force/strain[1].

Bottger et al. [41] and Dornfield et al. [42] have found devices monitoring AE capable of identifying process parameters such as tool condition, surface integrity and chip formation to a high degree of accuracy. Teti observes in separate papers that piezoelectric sensors are well suited to measuring AE [43], but also that they pose challenges of difficult signal data detection and processing [5]. AE sensors based on capacitance are said to be extremely accurate, but their sensitivity to positioning rules them out of harsh applications [2].

Temperature measurement for smart tooling is typically conducted using thermocouples [44]. K-type thermocouples were used by Maier et al. [45] for determining the temperature near the tool edge in milling, by Junge et al. [46] to assess temperature gradient near the chip formation area for turning, and by Wegert et al. [47] for drilling processes. Thermal imaging can also be used for temperature measurement, using infra-red radiation to monitor heat build-up in manufacturing processes as was done by Minora et al. [48]. However, the need to incorporate temperature-sensors within tools to detect conditions in the heated region is highly inconvenient and the tool adaptation often required to facilitate these can be prohibitive [2].

Vibration sensors have high potential for process monitoring due to their low cost and ease of implementation. Research has investigated the use of microphones [49] and accelerometers [50] for this purpose, with the latter proving the more versatile option. Vibration sensors can be used to detect chatter or tool imbalance [51], which is valuable because vibrations can significantly increase tool wear rates. However, vibration sensors require intensive feature extraction and are extremely sensitive to vibrations from the surrounding environment [50]. This rules out many industrial applications for these sensors.

Motor power and current have also been used for machining process monitoring, with spindle current data usually being used to approximate the cutting power of grinding machines [52], [53]. Typical power meters for motors measure voltage at the terminals and measure current via Hall Effect sensors [52], [54]. Li and Tso [55] conducted a study on how process parameters impact the electrical signal during drilling processes, finding a consistent relationship between spindle and feed motor current. Similarly, Kim et al. [56] used a Kalman filter disturbance observer and artificial neural network for feature extraction of cutting force signals during a multi-axis milling. Furthermore, Brazel [12] successfully quantified the cutting power required to grind specific sections of an orthopaedic implant, as is seen in Figure 2.1.

[1]Force and strain sensors will be investigated in Sections 2.2 and 2.3, with a particular focus on their application to grinding processes.

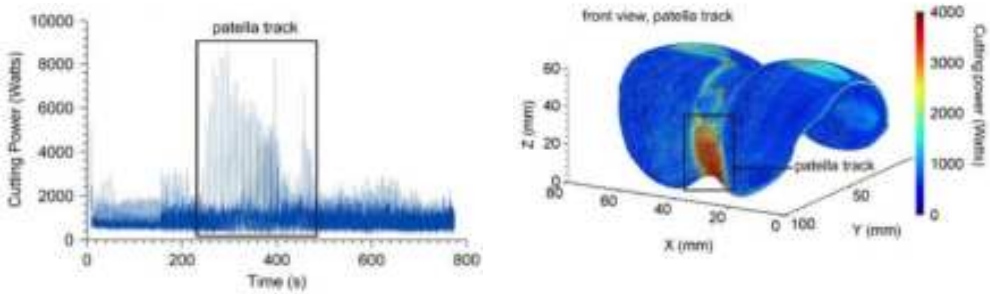

(a) Cutting power signal. (b) Cutting power map.

Figure 2.1: The use of cutting power for grinding process characterisation [57].

Teti et al. [2] highlighted a significant limitation to power and current based process monitoring as the data transmission rate of current is limited to less than 1 KHz, which is not sufficient to capture many system behaviours. This inability constitutes a significant gap in the method's process-monitoring capabilities.

Overall, a substantial gap exists between research into state of the art in smart tooling and its limited use in industrial scenarios [2]. System complexity and the use of non-standard tooling are the primary obstacles to the implementation of smart tooling systems [58].

2.2 Grinding Background and Monitoring

Grinding is a material removal process which involves an abrasive disc-shaped wheel rotating at high speeds to remove material from a workpiece. Grinding occurs on either the wheel face or wheel periphery, with the latter method being more common [59]. Grinding is the preferred machining method for many industrial applications where high-quality surface finishes are required. Applications range from the grinding of large lenses for astronomy down to that of tiny components for MEMS (Micro Electro-Mechanical Systems) [60]. Grinding is also used in the manufacture of aircraft engine components, such as high-pressure turbine blades [9]. The aviation industry is very tightly regulated, and grinding is the most effective way to achieve the required dimensional tolerances of less than $\pm 10\ \mu m$ [10].

A grinding wheel is usually made from a strong metal with abrasive grits adhered to the wheel periphery or is comprised fully of abrasive grit embedded in a binder. The former design is more common for high-precision applications [59], and typical abrasive materials used for this purpose include cubic boron nitride (CBN), silicon carbide and aluminium oxide [61]. Some industrial examples of grinding wheel compositions include electroplated steel wheels coated in CBN for the grinding of orthopaedic knee implants [12], and aluminium oxide abrasives for aircraft engine turbine blade grinding [10]. Wheels using lighter materials such as carbon fiber reinforced polymer are becoming increasingly available and can enable

wheel speeds of up to 200 m/min during operation [62].

Rowe divided traditional grinding processes into two main categories- flat surface grinding and cylindrical surface grinding [61]. Flat surface grinding (Figure 2.2(a)) is typically used to grind plain flat surfaces, by using the periphery of the wheel's flat face of the wheel to grind the workpiece. Cylindrical surface grinding (Figure 2.2(b)) involves the rotation of the workpiece, to allow for better generation of curved surfaces [59]. Cylindrical surface grinders are used primarily for creating cylindrical surfaces (although tapered and simple-formed geometries are also possible) [63].

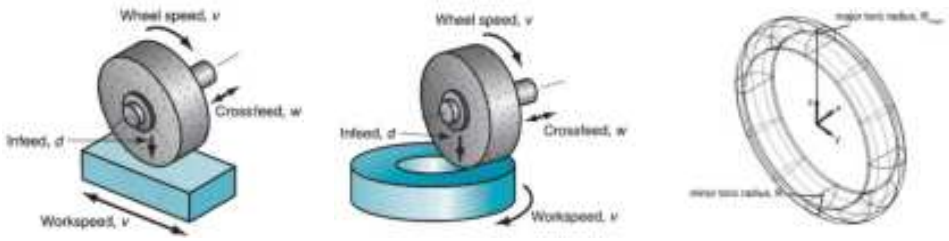

(a) (b) (c)

Figure 2.2: (a) Flat surface grinding [59] (b) Cylindrical surface grinding [59] (c) Toroidal grinding wheel. [12]

Freeform abrasive machining has become popular in recent years due to the wide range of workpiece geometries it can create. It is derived from traditional flat surface and cylindrical surface grinding, but its wheel movements are much less constrained. Freeform abrasive grinding machines typically utilise 3-6 axes of movement, allowing for production of freeform, complex-shaped parts. Toroidal wheels are typical of freeform grinding processes, these featuring a major radius extending from the wheel centre to its circumference, and a minor radius located along the circumference (Figure 2.2(c)). This allows generation of a greater range of geometries, by varying the orientation relative to the workpiece [64].

Other modern grinding developments include high-efficiency deep grinding (HEDG), ultrasonic-assisted grinding and nanogrinding [61]. HEDG is a form of grinding which is characterised by high work speeds and extremely high removal rates. Rowe and Jin [65] noted the method can achieve lower specific energy, lower grinding temperatures and lower thermal damage than slower grinding processes.

Ultrasonic vibrations are applied in ultrasonic assisted grinding to reduce the size of particles removed from the workpiece, leading to steady grinding forces, low workpiece sub-surface damage and reduced grinding temperatures [61]. Meanwhile, ultra-precision grinding (nanogrinding) machines are ones which achieve workpiece dimensions below the $\pm 1\ \mu m$ to $\pm 10\ \mu m$ accuracy range typical of conventional grinding machines. Yoshioka [66] performed nanogrinding by ensuring extreme accuracy in machine components such as the spindle, wheel shape and slide positioning (less than $\pm 0.1\ \mu m$).

2.2.1 Grinding Forces

The forces involved in grinding processes are typically resolved into two components- the normal grinding force (F_n) and tangential grinding force (F_t), both of which occur at the point of contact between grinding wheel and workpiece. The tangential force acts parallel to the workpiece surface, with the normal force acting in perpendicular to this (ref Figure 2.3). The normal grinding force (F_n) tends to be higher than the tangential force because of the effort required to press the wheel into the workpiece during operation (ref Table 2.1). Loads in the range of in the range of 36 N to 80 N are typical of normal grinding forces, with forces of 12 N to 42 N reported in the literature for tangential grinding forces.

Force also acts in out-of-plane (i.e. axial) directions in freeform grinding, but this is not well documented in the literature. Most studies mentioning axial grinding force (F_a) are ones which focus on axial ultrasonic grinding machines [67], [68], [69], [70]. These are grinding machines designed to vibrate in the axial direction during operation, which alters the axial force magnitude.

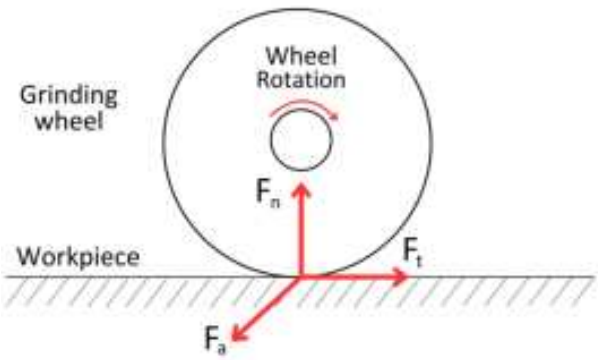

Figure 2.3: Grinding force components.

Tangential force (F_t)	Normal force (F_n)	Axial force (F_a)	Reference
42 N	80 N	n/a	[16]
12 N	36 N	n/a	[71]
35 N	85 N	n/a	[72]
21 N	59 N	n/a	[73]
n/a	n/a	74 N	[74]

Table 2.1: Peak grinding forces reported in a selection of academic papers. Unspecified force components are denoted by n/a.

Grinding forces tend to act through quite a small wheel-workpiece contact area, found to be in the range of 1-14 mm long by Qi et al. [75]. However, grinding forces and contact area can vary substantially, depending on factors such as grinding wheel surface speeds, wheel surface condition and depth of cut.

Olivera et al. [8] outlined significant challenges in modern grinding processes, namely ensuring surface integrity and process reliability, controlling wheel topography during operation and reducing energy consumption during grinding operations. Karpushcewski and Inasaki [9] also highlighted issues such as chatter[2], grinding burn[3] and workpiece stress concentrations in their keynote paper on grinding process monitoring. The challenges of residual workpiece stresses and grinding burn were similarly acknowledged by Klocke et al. [10] and Ceylan et al. [11] respectively. Finally, Brazel [12] notes the inefficiency of most grinding operations as operators typically tend to err towards conservative machining parameter choices such as feed rate to avoid workpiece damage. An effective process monitoring solution could help with this problem by providing machine operators with more information. Better knowledge of the system's state and behaviour would enable calculated process parameter adjustments which move away from the ultra-conservative approach and thereby make the process more economically viable.

The literature offers few examples of smart tooling designed for measuring force and/or strain in grinding wheels. Where such tools are mentioned, they are often located a considerable distance from the wheel-workpiece contact area, constraining the ability to effectively capture the system's behaviour. For example, Karpushewski and Inasaki [9] noted that force sensors are commonly affixed to the workpiece platform for the monitoring of surface grinding machines. An example of this approach is found in Liu's study [14] of strain gauges for measuring grinding and polishing forces with a rotary hand grinder (a grinding machine with a flexible arm and smaller tool piece). Figure 2.4 illustrates how the gauges were strategically placed on the platform supports to easily discern forces in the X, Y and Z directions and thus could identify the reaction forces between platform and ground.

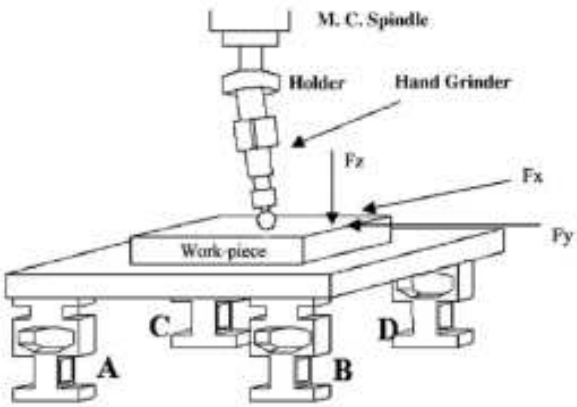

Figure 2.4: Strain gauges (labelled A-D) installed on grinding workpiece platform [14].

[2]Self-excited wheel vibration.
[3]Localised overheating of the workpiece.

A similar process was outlined in Lal's work [15], with strain gauges being installed on vertical workpiece platform supports. Each gauge corresponded to one of the three perpendicular force components, which were checked for cross-sensitivity.

In scenarios involving workpiece rotation, the absence of a workpiece platform necessitates alternative locations for mounting sensors. The viable options include the grinding wheel shaft, the workpiece shaft, and their respective supports—the tailstock and headstock. Strain gauges were applied to the head and tail stock by Onishi et al. [16], Yin et al. [17] and Walsh et al. [18]. The grinding wheel and workpiece shafts were less common sensor locations, due to their rotational movement, which posed a challenge for the use of wires and, consequently, strain gauges. An additional disadvantage of strain gauges for this purpose is that they are not sensitive enough to facilitate comprehensive monitoring of grinding forces. Significant system stiffness reductions are often required to ensure that strain is detected in the grinding wheel or machine [9], leading to wheel deflection which is detrimental to dimensional accuracy[4].

Commercial cutting force sensors mostly tend to consist of piezoelectric dynamometers, as were used to measure tangential and normal internal grinding forces by Tonshoff et al. [76] and cyclical grinding forces by Kita et al. [77], with both methods achieving limited results. Tonshoff's dynamometer system was not effective for anything beyond the first cut and Kita's worked only for grinding wheels transitioning from high velocity to an abrupt stop. Bhowmick et al. [78] and Zhang et al. [79] also worked to develop novel dynamometers for grinding, but both solutions were quite bulky and intrusive, making them ineligible for applications near the wheel-workpiece contact area. This limits the sensors' process monitoring capabilities, as measurement close to the contact zone is required to enable precise observation of the grinding process [19]. Embedded strain sensors represent a possible solution to the problem; these are discussed in Section 2.3.

2.3 Strain Theory and Measurement

Strain, denoted by ϵ, quantifies a body's deformation when subjected to a load. It is defined as the ratio of its change in length (ΔL) to its original length (L), as per Equation 2.1 [80]. A positive strain value signifies that the body is experiencing tension, whereas a negative value indicates compression. Although strain is dimensionless, it is typically expressed in units such as m/m, mm/m or μm/m. The relationship between strain and stress (σ) in a body is described by Equation 2.2, highlighting that strain is directly proportional to stress and inversely proportional to the Modulus of Elasticity of the body's material (E) [81].

[4]Strain gauges will be discussed further in Section 2.3.

$$\epsilon = \frac{\Delta L}{L} \quad (2.1) \qquad E = \frac{\sigma}{\epsilon} \quad (2.2)$$

Here, stress is calculated as the force (F) applied to the body divided by the area (A) over which the force is distributed [82]. By integrating equations 2.3 and 2.2, we achieve a more comprehensive expression for Modulus of Elasticity in terms of applied force, area, and strain (Equation 2.4).

$$\sigma = \frac{F}{A} \quad (2.3) \qquad E = \frac{F/A}{\epsilon} \quad (2.4)$$

This equation illustrates that for constant values of area and Modulus of Elasticity, the strain in a body is directly proportional to the force applied to it. Thus, the forces acting upon or within a body can be inferred by analysing the strain it exhibits. A practical application of this relationship would be to measure strain in a grinding wheel so as to calculate the forces acting on it.

2.3.1 Traditional Strain Sensing Technologies

Traditional strain sensing technologies can be divided into four main categories- piezoresistive, capacitive, piezoelectric, and strain gauge sensors. Piezoresistive, or semiconductor, strain sensors operate based on the piezoresistive effect where the electrical resistivity of a conductor changes under applied mechanical stress. Piezoresistive sensors tend to be cheap, stable and require minimal maintenance, although they offer a restricted measurement range and low sensitivity. These sensors are also affected by electromagnetic interference, which is unsuited to industrial applications [83].

Capacitive strain sensors incorporate an insulating material (or dielectric layer) between two metal electrodes. The capacitance (ability of the sensor to store charge) is based on the geometry and spacing of the electrodes, so it changes when mechanical strain is applied and the spacing is altered [84]. Capacitive strain sensors offer several advantages, including high resolution, wide bandwidth, low noise, and a large dynamic range. Capacitive-type sensors were also shown to require less power [85] and to be less prone to hysteresis than resistive-type strain sensors. However, they provide limited sensitivity, and their accuracy can suffer from temperature variations and hysteresis [86].

Piezoelectricity is a mechanism where electrical voltage is directly generated under mechanical deformation, triggered by the electrical dipole moments (separation of positive and negative charges) in piezoelectric materials [87]. Piezoelectric strain sensors are typically incorporated into a circuit with charge amplifiers, to strengthen the signal and allow it to be used for strain measurement. The sensors tend to be compact, display high sensitivity and

fast response times [86], whilst being effective over a large strain bandwidth. Piezoelectric sensors also offer simultaneous multi-strain detection but require additional interrogation and processing hardware [88].

Strain gauges stand as the predominant strain measurement method at present, being used in over 50% of all strain sensing applications [31]. They are reliable components which offer simplicity of installation and operation, making them a favored choice for experimental analysis [3]. The metal foil strain gauge, a resistive-type strain sensor, represents the most commonly used variant of this sensor type. Its functionality relies on the strain/resistance relationship inherent in electrical conductors, whereby the resistance of a conductor changes as it undergoes deformation from applied mechanical stress [84]. The resistivity change is caused by changes in cross-sectional area for metal foil strain gauges, in contrast to piezoresistive sensors which instead undergo resistance changes due to electron mobility.

Proper strain gauge installation is crucial for their correct functioning, and Masláková et al. [89] provide a thorough guide for the process of attaching a strain gauge to a workpiece. The application area is first subjected to a specific sanding process, followed by a solvent cleaning process to remove contaminants before the strain gauge is affixed to the prepared surface. Hoffmann [90] noted that strain gauges are commonly affixed to the test object using adhesives, although spot-welding and ceramic materials can also serve this purpose. Adhesives offer versatility by facilitating bonding across a wide range of materials and efficiently transferring strain from the test object to the sensor. Quick-setting adhesives prove valuable in this context, as their accelerated curing times enable swift application.

The thickness and composition of the selected adhesive play a crucial role in influencing strain results, with thicker adhesive layers demonstrating inefficiencies in transferring strain between the test piece and strain gauge. However, the impact of adhesive layer thickness appears to be less pronounced when measuring strain under larger applied loads [91].

Three types of adhesives are commonly discussed in the literature regarding strain gauge application, namely cyanoacrylate, polyurethane, and epoxy-based adhesives. Komurlu et al. [92] identified cyanoacrylate adhesives as the most effective among these substances for strain gauge installation as they form thinner layers, resulting in more accurate measurements. In turn, epoxy-based adhesives have been demonstrated to be more accurate than polyurethane agents [91].

Strain gauges are commonly implemented with the use of a Wheatstone bridge, a particular electrical circuit design into which the strain gauge is incorporated [90]. The strain gauge acts as a resistor in the circuit and when strain induces a resistance change, the bridge becomes unbalanced. The bridge output voltage is proportionate to the degree of unbalance

so it can be recorded and converted into strain readings after amplification[90].

Wheatstone bridges come in three configurations- quarter bridges (as seen in Figure 2.5), half bridges, and full bridges, incorporating one, two, or four strain gauges, respectively. The decision on which bridge to use involves a trade-off between the number of output signals and the required sensitivity. Each Wheatstone bridge provides a single output signal, so incorporating multiple sensors into one circuit does not yield additional streams of information. However, the addition of extra strain gauges to the bridge enhances its sensitivity. For example, a full bridge configuration, is twice as sensitive as a half bridge when measuring bending moments according to McLoughlin et al. [93]. Consequently, one full bridge can sometimes achieve the same sensitivity to strain as two half-bridges.

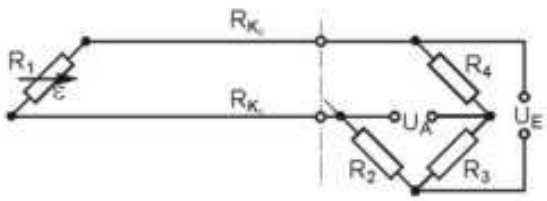

Figure 2.5: Quarter bridge circuit for strain measurement [94].

Strain gauge output signals often contain noise that needs to be separated from the true signal to achieve accurate measurements. Data averaging can be used to reduce signal fluctuations due to noise if measurement conditions are static, but the technique cannot be applied during dynamic processes [95].

Another significant limitation of strain gauges is their characteristic of only providing a single-point measurement- strain is only measured within a small area and in a given direction [3]. Therefore, it is essential to position strain gauges accurately; they need to be meticulously aligned at the best possible angle on the specimen to precisely measure strain patterns. Strain gauges perform most effectively in regions exhibiting uniform strain, where there is more margin of error in strain gauge placement.

The optimal locations for applying strain gauges vary depending on the geometry and loading conditions of the test object. For instance, one strain gauge is sufficient when dealing with strain caused by a single bending load, but two are needed if there is also an axial load. In cases of applied torsion on shafts, strain gauges are frequently used to record strain on the shaft's circumference. A common rule of thumb is to install these gauges at a 45-degree angle to the shaft axis, as this tends to align well with the principal strain direction [96].

One option that addresses positioning requirements is the rosette strain gauge. These include several measurement grids on the one carrier, which are oriented in different

directions. Each measurement grid produces a separate output signal, so more information can be obtained. Various commercially available variations include the tee, delta, and rectangular rosettes, which are shown in Figure 2.6.

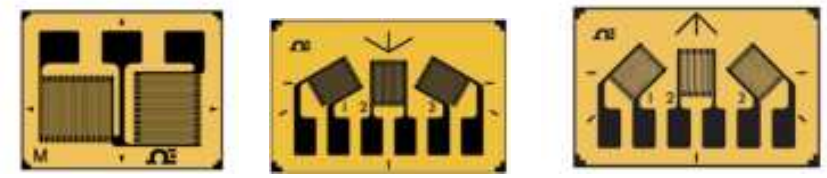

(a) Tee rosette [97] (b) Delta rosette [98] (c) Rectangular rosette [99]

Figure 2.6: The three basic types of rosette strain gauge.

2.3.2 Novel Strain Sensing Technologies

Various categories of innovative strain sensors are currently under research, showing potential for embedding them into host structures. The key feature of embedded sensors is their capability to be deployed in-situ, meaning they can be positioned in close proximity to the objects they are sensing [4]. Passive sensors, which do not require a power source [7], are well-suited for this purpose, eliminating the need for bulky battery packs or power cables. While much of the current research on embedded strain sensors has focused on wearable applications [86], [100], the potential applications of smart tooling in the manufacturing industry have also gained attention.

Hamed et al. [31] conducted an extensive review of the current state of novel strain sensor technologies, identifying Fiber Bragg grating, Magnetostrictive, and Surface Acoustic Wave sensors as the most promising technologies. Each of these sensor types holds the potential for embedding in test specimens and could prove highly valuable in industrial manufacturing.

Fiber Bragg Grating (FBG) sensors function by absorbing and reflecting different wavelengths of light, and this interaction is influenced by physical parameters like temperature and stress. Analysing the wavelength changes in these sensors allows for the determination of property changes, such as mechanical strain [101].

Compared to traditional strain sensors, FBG sensors offer superior sensitivity, lower attenuation, and a broader bandwidth. They also provide immunity to electromagnetic interference [101] and are these sensors are well-suited for demanding environments, including high temperature, high pressure, and ionizing radiation, due to their passive, batteryless operation [102]. Furthermore, FBG sensors are capable of measuring extremely low strain values- Quintero et al. achieved a strain resolution of 0.8 $\mu m/m$ with FBG

sensors [103][5].

Despite their advantages, FBG sensors tend to be bulky and involve challenging installation procedures, requiring complex interrogation and data processing systems that can be expensive [104]. Additionally, their inherent fragility and their dependence on a physical broadband light source make them unsuitable for many industrial applications [105].

Magnetostrictive (MR) strain sensors operate based on the Villari effect, which is the tendency of certain materials, referred to as magnetostrictive materials, to experience mechanical strain when exposed to a magnetic field [84]. The Villari effect, the inverse of magnetostriction, indicates that when MR materials undergo strains, the direction and magnitude of the measured magnetic field are affected [106], making them suitable for strain measurement applications.

MR sensors offer high bandwidth and rapid response across a diverse range of frequencies [107]. They do not require a coupling medium, eliminating the need for direct physical contact [108]. Noteworthy advantages include feasible installation processes, simple data acquisition hardware, and the ability to operate passively, making them suitable for applications in hard-to-reach locations [106], [109]. Furthermore, MR sensors have measured strains in the range of 1-10 $\mu m/m$ [110], so are capable of detecting extremely small strain changes. MR sensors with passive operation are already visible in fields such as biomedical engineering [111], [112], robotics [22], and materials engineering [113].

MR sensors also have drawbacks, including lower sensitivity, reduced accuracy [31], susceptibility to magnetic interference, and complex signal drift at elevated temperatures [106]. These factors have limited the use of MR sensors in industrial applications so far.

Surface Acoustic Wave (SAW) sensors constitute an innovative category of sensing technologies and emerge as one of the most promising devices for strain measurement. These sensors operate based on piezoelectric materials that generate acoustic waves on the surface of the test material when an electrical signal is applied [114]. The application of strain to a SAW sensor results in frequency, velocity, and/or amplitude shifts in the reflected signal, which are indicative of changes in substrate geometry. The reflected acoustic waves are captured by the reader antenna and analysed to extract strain measurements corresponding to induced loads [115].

SAW sensors leverage high frequency, piezoelectric properties, and low-loss characteristics, demonstrating resilience in extreme conditions like weather, radiation, and shock. With rapid readings taking only a few microseconds, they allow for over 10^5 interrogations per second [116] and exhibit extremely high sensitivity to physical properties such as strain and

[5]Note that this is not a universal value, as strain resolution varies according to the interrogation system used.

temperature [27]. Their compact size, cost-effectiveness, insensitivity to magnetic fields, and suitability for wireless installation on moving or rotating parts make them advantageous for industrial applications [7]. SAW sensors are extremely sensitive to strain changes, having been reported to achieve strain resolution values of as low as 0.2 $\mu m/m$ [117]. Previous studies have explored their wireless deployment on components such as marine propeller shafts [23], automotive tire monitoring systems [7], and robotics and microfabrication devices [118].

The use of SAW sensors presents challenges, as they demand complex packaging and installation specifications [119]. Additionally, the data derived from SAW sensor measurements require advanced signal processing techniques such as machine learning algorithms [120]. Furthermore, the intricate behaviours and operational intricacies of SAW sensors necessitate additional research before their widespread adoption. Notably, industry standards for the calibration of SAW sensors are yet to be established, although some calibration approaches have been proposed in the literature [121], [122].

2.4 Grinding Wheel Analysis Using In-Plane Torsion Testing

Most existing analytical and FE models aiming to represent the forces and stresses in the grinding process tend to delve into intricate details, including factors as minute as the thickness of individual grains of abrasive grit bonded to the grinding wheel [71], [73], [123], [124]. However, Herzenstiel et al. [19] proposed a more simplified grinding system representation, applicable to both computer models and experiments to replicate real grinding. In this simplified view, the contact force transmission between the workpiece and the wheel can be averaged out over the contact area, eliminating the need to calculate for individual abrasive grits. It was similarly observed that the grinding system can be reduced to an analysis of stationary bodies if assumed to be in equilibrium, i.e. if the grinding wheel is assumed to rotate with a constant angular velocity and to generate constant grinding forces. Wheel velocity and cutting force fluctuations are obviously common in real grinding processes, but this constitutes a practical, reasonable assumption to make force analysis more manageable. By extension, a flat disc can be used as a substitute for the toroidal shaped geometry which is typical of grinding wheels.

If these deductions are deemed reasonable, then the experiments known as "in-plane torsion tests" may be regarded as indicative of the grinding process conditions. Initially outlined by Tekkaya et al. [125], these tests typically involve a disc being held at its periphery by clamping tools, while torsion is applied to the disc by an inner rotating shaft. This testing method has been widely used in various studies analysing shear fracture mechanisms in

metal discs. However, challenges arose due to the necessity for applying high torques and the difficulty in measuring stress and strain, due to their localisation near the inner clamping area [126].

Brosius et al. [127] introduced a modified version of the in-plane torsion test to address these challenges, known as the twin bridge shear test. In this test, grooves were cut into the top and bottom faces of a 2 mm thick steel disc, with the grooves separated in two places. This design resulted in the creation of gauge sections, known as shear bridges, in the angular intervals ranging from -10 degrees to 10 degrees and from 170 to 90 degrees (Figure 2.7(a)). The disc thickness was reduced to a minimum of 0.3 mm at the groove locations. The inclusion of grooves significantly lowered the torque required to induce substantial shear stresses in the disc by concentrating strain in a narrow band around the groove. This adjustment made the strain more detectable, facilitating more accurate measurements.

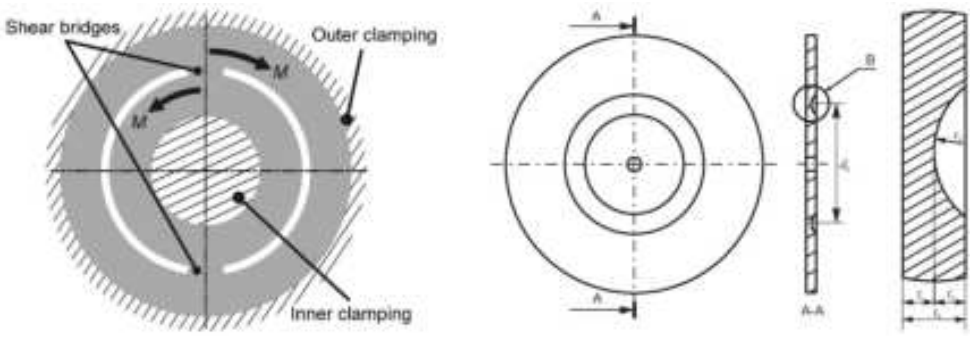

(a) (b)

Figure 2.7: (a) Twin-bridge setup (b) Grooved disc setup for in-plane torsion testing.

Yin et al. [126] further refined this method by eliminating the gauge sections, cutting a circumferentially uniform, unbroken groove into a steel disc (see Figure 2.7(b)). The disc had an initial thickness of 1.55 mm, which was lowered to a minimum thickness of 0.7 mm at the bottom of the groove. The modification aimed to provide more uniform stress and strain patterns for easier identification and analysis. Extremely high torque values (up to 1100 Nm) were applied in this test, resulting in disc slippage relative to the clamp. Surface corrugation was then successfully introduced to the clamping surfaces for additional friction, which was achieved by engraving 1 mm pyramids onto the clamp. Stress and strain concentrations were also noted to occur at the grooved section in this test.

2.5 Strain Modelling and Validation

The Finite Element (FE) method is often used to calculate the optimal strain gauge position and orientation for installation on test specimens. This method involves the discretisation of differential equations for problems in areas such as structural dynamics, which enables approximations of their solutions to be calculated [128].

The use of FE modelling and strain gauges in tandem appears often in the literature. Banther et al. [24] developed a FE model to analyse the dynamics of a motor vehicle suspension, predicting strain distribution within the system. A numerical search algorithm was then used to determine the optimal gauge position and orientation for strain sensitivity. Another study by Lertchirakarn et al. [25] went further than this by later validating their FE models of dental structures with strain gauge measurements at specific locations. The FE model was found to have accurately predicted tensile and compressive strain in the areas of interest. However, the comparison was purely qualitative as the absolute strain values for both sets of results were not directly compared. By contrast, Chen et al. [26] validated their FE model of a hole under stress in quantitative terms; the numerical results were found to have an average precision of 95.4%, indicating a high degree of realism associated with the FE model.

Kalinan's research [23] into the feasibility of embedded Surface Acoustic Wave (SAW) sensors for torque measurement in marine propeller shafts is also pertinent to this project. It used a similar approach to the other studies, in that it used experimental measurements for verification of an FE model. The predicted and measured strain values were then compared, revealing a discrepancy of just 3.1%. Following this validation, the SAW sensors were installed on an operational propeller shaft and successfully monitored a passenger ship's operational torque output.

Despite the prevalence of FE modelling in the literature, few examples exist which are relevant to strain in grinding wheels. Models have been created which analyse workpiece stresses [129], [130], [131], but no papers focusing on the stress or strain behaviour of the grinding wheel itself have been identified.

There are examples of FE modelling for objects with similar geometries and loading conditions, with disc brakes being the most comparable to the grinding setup. Belhocine [132] notes the maximum stresses to occur at the wheel periphery, near where the brake pad clamps onto the disc. Manjunath and Suresh's paper agrees with this, indicating that the maximum wheel deflection due to applied torsion occurs at the wheel exterior. Grzes and Kuciej's work [133] further correlates with this, indicating maximum stress underneath the brake pads.

2.6 Summary

This chapter details the current state of the art in smart tooling, emphasizing its potential to bring about improvements in the manufacturing industry. It focuses especially on sensors suitable for integration into machine tools, prioritising compactness and wireless functionality. A significant gap was observed in the area of grinding process monitoring, where current practices lack a method for measuring force in industrial grinding wheels during operation. This forces a reliance on trial-and-error for setting parameters like feed rate and depth of cut, which can negatively impact product quality and manufacturing efficiency. The problem constitutes a research opportunity, the solution to which could be particularly valuable in sectors requiring precise tolerances like the aerospace industry.

Attempts to date at grinding force measurement have primarily relied upon dynamometers which are bulky and intrusive, preventing their use close to the grinding wheel-workpiece contact area. Strain sensors have also been used to infer grinding forces, with strain gauges being used to monitor forces by attaching them to the workpiece platform. However, this placement is not optimal as it is also removed from the contact area. Other traditional strain sensing technologies like piezoresistive and capacitive sensors are unsuitable for measuring forces in moving grinding wheels due to their inability to accurately capture dynamic stress changes and their physical limitations in the harsh grinding environment.

Some novel strain sensing technologies have demonstrated potential for embedded grinding force measurement, primarily SAW, and MR sensors. The passive operation of SAW and MR sensors opens the possibility of integration into grinding wheels, thereby offering a direct method for measuring forces within the wheel. Nonetheless, these novel sensors require further research and development before implementation, especially regarding the establishment of reference measurements for accurate calibration and validation. Crucially, further research is required to understand how strain develops in grinding wheels before the sensors can be used in this context. The project sets out to address this knowledge gap by observing the strain patterns present in grinding wheels and determining if these can be exploited by embedded sensors for force measurement.

3 Simplified Disc Structure: Experimental Approach

Chapter 3 details the general experimental methodology used throughout the project. It initially outlines the general approach taken in the project, before introducing three simplifications made to the grinding setup to facilitate strain measurement. Following this, the general experimental techniques applied to mechanical testing are outlined. An explanation is subsequently given of the approach taken to create a Finite Element (FE) model for strain prediction in grinding wheels and similar geometries. The chapter then concludes with a high-level outline of the three principal areas of investigation in the project.

3.1 Simplifications To Grinding Setup

Three practical simplifications were adopted in this project to allow the creation of experimental setups which were analogous to real grinding processes. They represent practical measures which allow the measurement of strains typically present in a grinding wheel in operation, without monitoring the wheel in action.

The first of these was the simplification of a grinding wheel in motion down to that of a wheel under static loading, Figure 3.1(a) to Figure 3.1(b). By assuming that the grinding wheel operates in equilibrium, it becomes feasible to analyse its strain and force behaviour under static loading conditions i.e. in-plane torsion testing. A torsional moment is applied to the disc's interior to replicate the torque provided by the grinding wheel shaft and a clamp is fixed on the wheel's periphery to mimic the workpiece reaction forces typically acting on the wheel. Shear strain develops on the disc top and bottom surfaces due to the loading conditions, which can then be measured, analysed and used to determine if there is potential for embedded strain sensing in grinding wheels. It was assumed that no out-of-plane (i.e. axial) forces would be present, so no bending strain was expected here.

A second simplification was made to the grinding wheel setup, a reduction of the wheel geometry down to that of a flat disc which has two effects. The first effect is that the wheel's reaction to forces is distilled down to the core strain behaviour present in its most basic geometry (i.e. the flat disc). This has the benefit of making the project findings applicable to a wide variety of grinding wheel geometries e.g. not just the toroidal grinding wheel used for freeform machining. The second effect was that the shear strain response of the flat disc was expected to be simpler to record and analyse, thereby increasing the

probability that useful observations could be made during the project.

The third and final simplification made in this analogy was to reduce the disc geometry down to a small segment of the disc (Figure 3.1(b) to Figure 3.1(c)). By analysing just one segment of the beam geometry (i.e. a thin beam), it became possible to compare the strain against analytical calculations from simple bending theory. This was achieved by clamping a beam at one end in a test rig and applying a force to the other. The force generated a torsional moment due to its distance from the fulcrum, so it was therefore subjected to torsion like a segment of the disc during torsion testing. As such, the beam was expected to display comparable shear strains to a disc segment under torsion testing. This allowed the project to analyse the maximum achievable accuracy in the grinding strain measurement scenario, and to determine where experimental error may arise in the project results.

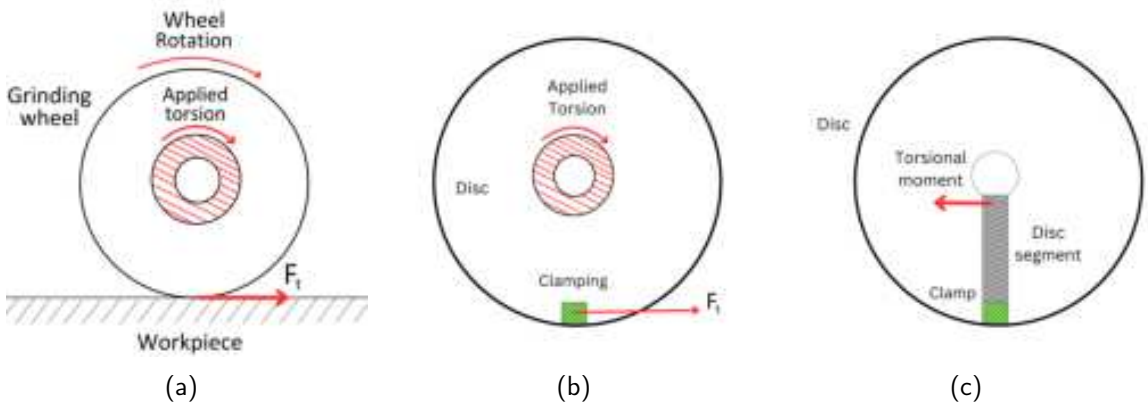

Figure 3.1: Schematic diagrams of a) grinding wheel in motion b) disc under torsion c) disc segment under torsion.

3.2 Strain Measurement

Strain gauges were the primary sensor type used to obtain strain measurements during static loading tests throughout the project[1]. Their selection was primarily based on their ease of installation, ease of operation, and high reliability. Key considerations in the application of strain gauges include meticulous preparation of the test piece surface, appropriate adhesive selection, and ensuring the correct amount of adhesive is applied.

3.2.1 Strain Gauge Application

CEA-series tee and rosette strain gauges strain gauges from Micro Measurements were used throughout this project. The strain gauge application process began with preparation of the target surface. The gauge application site was initially sanded to ensure a smooth surface-

[1]A Kistler sensor was also used in one experiment- see Section 5.3.1.

first with 220 grit sandpaper, then with 320 grit paper. The surface was then treated with Acetone solvent to degrease the surface and remove particulate impurities. A gel-based cyanoacrylate glue (Loctite 454) was then used to bond the strain gauge to the target surface, pressing down with wax paper and rubbing it to remove any air bubbles beneath the sensor. Solder pads were glued to the workpiece and connected to the gauges with individual strands of wire (AWG 38). Next, thicker wires (AWG 24) were soldered to these pads and braided together for tidiness. Finally, the wires were taped down near the sensor positions, to ensure that wire movement would not transfer to the gauges and break the soldered connection.

3.2.2 Data Collection

The strain gauges were connected to a National Instruments NI-SCXI-1314 module, which was installed on a National Instruments PXI-1011 chassis. Each strain gauge was integrated into a quarter bridge circuit, with individual gauges allocated to separate channels on the module. LabVIEW 2009 software facilitated the recording of strain gauge measurements, which were recorded at a frequency of 25 Hz. An inbuilt calibration feature was used to zero the strain readings at the initiation of each set of tests. This calibration process effectively countered thermal effects and residual stresses in the strain gauges and lead wires, thereby baselining the collected data.

The quarter bridge configuration was selected over half and full bridge setups due to its ability to provide distinct signals from each individual sensor. This decision stemmed from the expectation that having a greater number of strain signals would offer a more comprehensive understanding of how strain evolved within the disc. While this choice does come with a trade-off in sensitivity, it was anticipated that the strain values would vary significantly across different positions. Therefore, using a half bridge setup with only two gauges, or a full bridge setup with four bridges, to calculate an "average" strain could potentially yield inaccurate results, as these configurations assume uniform strain (which may not be the case in this scenario).

A significant level of noise was present in the strain gauge signal; a 30 point moving average was applied to counter this. The technique involved calculating an adjusted range of strain gauge measurements, where each data point was taken to be the average of the 30 data points before it, thereby lessening fluctuations from the original strain signal. This technique is valid because the tests were all static loading studies. However, the use of moving average required careful consideration when applied to dynamic strain measurements to avoid the elimination of fluctuations of interest [95].

3.3 Torsion Testing

3.3.1 Grinding Wheel and Discs

A toroidal-shaped grinding wheel, typical of the freeform grinding process, is the focus of this thesis. The sample wheel that the project focuses on is made from high carbon steel and has a layer of cubic boron nitride (CBN) covering its periphery (Figure 3.2)[2].

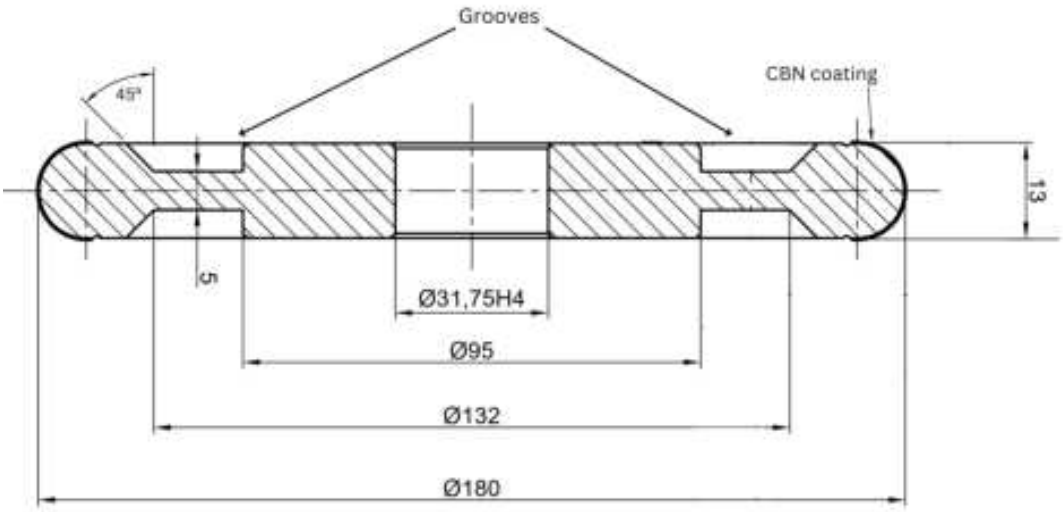

Figure 3.2: Grinding wheel cross-section.

Simplified thin discs were also used in this project, these being more susceptible to strain and thus more accommodating of strain measurement. The grooved sections cut into the grinding wheel (ref Figure 3.2) were not replicated in the manufacture of these discs, to ensure simpler strain patterns which would be easier to analyse. A 50 mm wide segment (ref Figure 3.1(c)) was ground on the top surface of each disc, producing a smoother surface finish which would facilitate optimum strain gauge adhesion. These discs were 5 mm thick and 3 mm thick respectively, with both made from low carbon steel.

3.3.2 Test Rig

The torsion testing for this project was conducted with an Instron 8874 Biaxial Testing System, with the capability to apply up to 25 kN of force and 100 Nm of torque to samples. Custom components were fabricated to enable the Instron to apply torque to the disc, including washers and a mandrel bolted to the disc using an M10 nut. The rotating actuator was secured onto the top of the mandrel so that torque applied from the machine was transmitted through the washers and onto the disc, as seen in Figure 3.3. This torsional load was applied about the vertical axis in a clockwise direction.

[2]The CBN layer was not factored into the simulations, as it was not expected to have any effect on the wheel behaviour under the applied experimental conditions.

A holding force was applied to the disc via clamps, which would simulate the reaction forces provided by a workpiece during grinding. These were positioned at the disc periphery and were affixed to T-slots in the Instron base. By immobilizing rotation about the vertical axis, the clamps ensured that the disc remained stationary when torsion was applied from the Instron actuator, thus establishing a static loading scenario which would facilitate strain analysis.

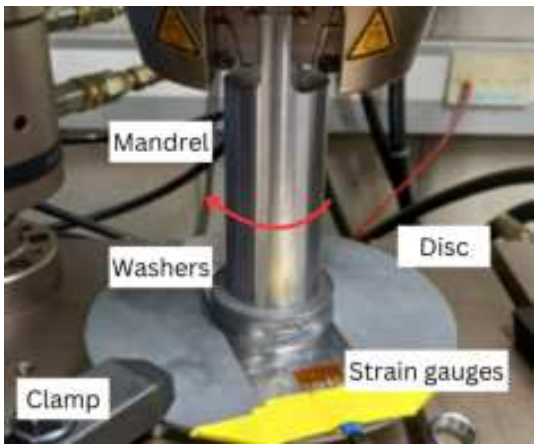

Figure 3.3: Use of custom components in torsion testing setup.

3.3.3 Static Loading Procedure

The setup procedure for each set of torsion tests commenced by securing the mandrel in the Instron actuator grips and adjusting the actuator until the disc reached clamp level. The disc was then firmly clamped in place, and the Instron axial load (force in the vertical direction) was zeroed. Torsional loading cycles were subsequently initiated using Bluehill software, and the resulting strain levels were recorded using LabVIEW.

The torsional load was subsequently applied through the actuator, gradually increasing to the desired torque level over a period of 5 seconds. This maximum torque was then held constant until the strain gauge signal was deemed stable, before a 5 second return to idle conditions was implemented. 3 loading cycles were conducted for each test, with the first building up to a maximum torque of 10 Nm, the second to 20 Nm, and the third to 30 Nm.

3.4 Finite Element Model

FE modelling was used in this project to predict forces and strain in grinding wheels under typical operating conditions. These models were to be validated with static loading tests which applied torsional loads analogous to those applied in real grinding processes. Once validated, the models could then be used to determine if embedded strain sensors have

potential for force measurement in grinding wheels.

The geometry and material properties of the components being modelled are important input parameters which must be applied correctly to ensure accurate simulations. The choice of an appropriate mesh and the proper definition of contact and boundary conditions are similarly important, with each factor having a significant effect on the strain predictions. The strain gauge dimensions and positioning were recorded during mechanical testing. These were then used to create solid models of the grinding wheels and flat discs in SolidWorks 2022, which were subsequently transferred to ANSYS Workbench 2023 R1 for meshing. Finally, static structural studies were conducted using the ANSYS Mechanical interface, yielding predictions of induced strain in the wheels and discs.

Most of the foundational FE model work in this project involved simulations of steel discs under torsion. As such, the forthcoming discussions of the general FE process refer to discs and not grinding wheels. FE simulations of grinding wheels were conducted in later work; these are discussed in Chapter 6.

3.4.1 Geometry and Properties

The disc geometry was accurately modelled based on the dimensions measured during testing. This was represented as a solid body on which strain gauges made from shell elements were attached. The mandrel, washers and clamps were not modelled as solid objects- the effects of these components were instead accounted for in boundary conditions later applied to the model.

Symmetry is often used in FE modelling to streamline computational costs by analysing only a fraction of the whole geometry, thereby reducing computational requirements. However, this approach is suitable only when uniform and symmetrical behaviour is expected across the lines of geometrical symmetry. Asymmetrical strain behaviour was expected from the disc in this project, so this approach was not taken here.

The disc material properties were accounted for in the simulations by assigning the AISI 1010 carbon steel material to them. The other (high carbon steel) objects simulated in this project were represented with the assignment of AISI 1340 carbon steel material properties. The default material properties in the ANSYS library were used here[3]. There was a possibility that the disc's elastic limit would be surpassed during testing due to the application of high torsional loads, so non-linear material deformation was enabled in all simulations.

[3]See Appendix A2.

3.4.2 Mesh

Higher order tetrahedral (Tet 10) elements were used to mesh the disc model, as seen in Figure 3.4. The choice of higher order over first order elements enabled stress and strain calculations throughout each element, rather than solely at the element nodes. It offers greater precision in exchange for increased computational requirements and longer solution times [134].

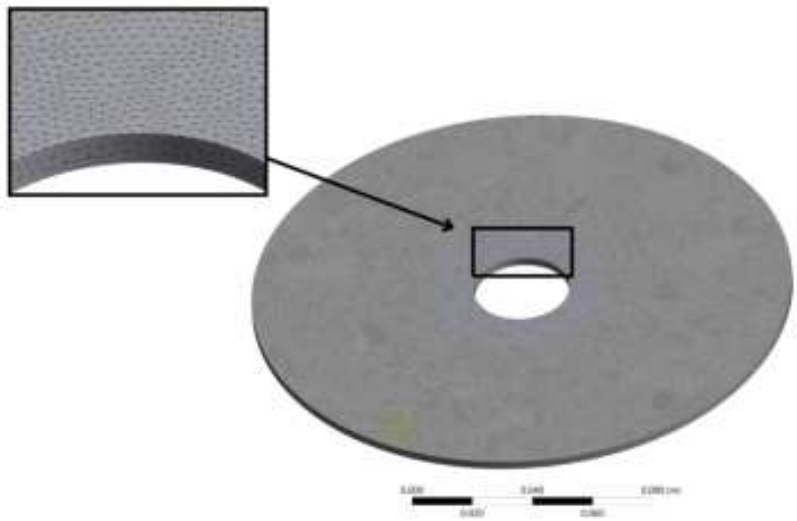

Figure 3.4: Finite element mesh for 3 mm disc model.

Mesh parameters	
Mesh type	Tetrahedral
Element order	Higher order
Num. elements	112,953
Num. nodes	201,772
Mesh size	1.5 mm

Table 3.1: Finite element model mesh parameters.

The decision to use a tetrahedral mesh was based primarily on the results of a mesh convergence comparison (Figure 3.5(a)). It demonstrated the fastest convergence among the available mesh types in ANSYS, indicating better result consistency and thus better simulation precision[4]. The tetrahedral mesh convergence was then analysed to determine the optimum global mesh size, with mesh independence being achieved at a global mesh size of 1.5 mm.

[4]Note that although mesh convergence indicates good precision, it doesn't guarantee simulation accuracy.

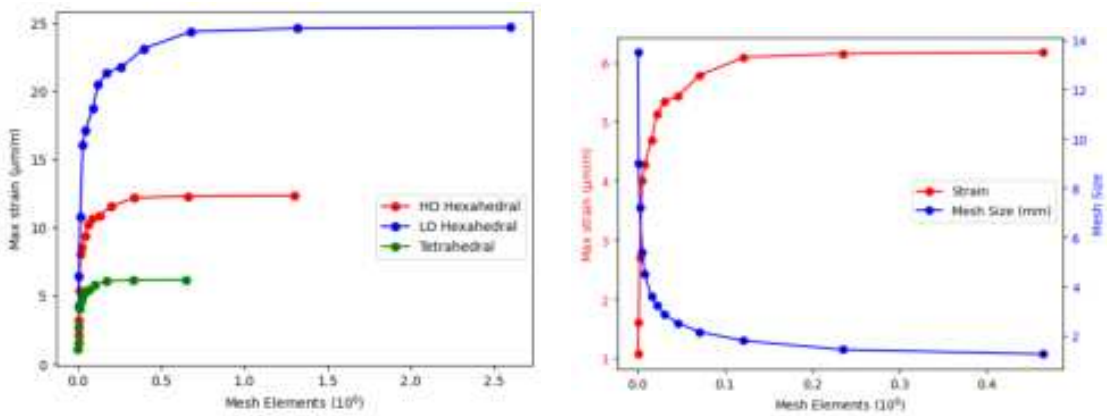

(a) (b)

Figure 3.5: (a) Mesh type convergence comparison (b) Mesh independence analysis.

3.4.3 Boundary Conditions

The mandrel and washers were assumed to transfer the torsional load between the Instron and disc both completely and uniformly, with negligible component deflection and no torsion loss due to slippage. As such, the geometries of these components were not incorporated in the model. Their effects on the experiment were instead reflected with the application of boundary conditions- a torsional load was applied where the top and bottom disc surfaces met the washers, as seen in Figure 3.6. The torsional loads acted about the vertical axis Boundary conditions were similarly used for the modelling of clamps on the disc periphery, with a fixed support being set up at each of the clamp-disc interfaces. These constrained the interface areas from vertical and horizontal translations, as well as constraining rotations at these points.

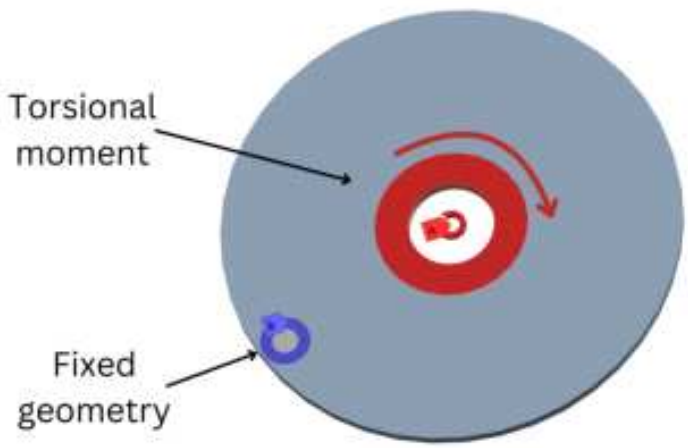

Figure 3.6: Finite element model boundary conditions.

3.4.4 Strain Gauges

The strain gauges were simulated as shell elements on the target surface (i.e. the disc), a technique which achieved 99.98% accuracy for a recent comparison of strain gauge modelling methods [135]. Shell 181 elements were chosen here because they account for transverse shear stresses, which were expected to be generated in the disc by the torsion applied to it. Bonded contact interfaces were defined between the sensors and disc in the model to reflect the adhesive bond between the real-life components. The disc was selected as the target body, with the strain gauges being assigned as the contact body. This definition ensured that any strain observed in the disc would be perfectly transferred to the strain gauge, but no strain would be carried in the opposite direction. The strain gauges were subsequently assigned zero stiffness using ANSYS parametric design language (APDL) commands because strain gauge stiffness is considered insignificant when bonded to much stiffer bodies [136].

3.4.5 Simulation Output

The FE model output was analysed with two main tools on ANSYS- the Normal Strain and Construction Path features.

The strain across each strain gauge element was computed and extracted through the Normal Strain feature. Local coordinate systems were established for each strain gauge, facilitating the calculation of this along the longitudinal axis of the gauges. This method was consistently applied throughout the project to anticipate the strain value at specific points in a designated direction, such as predicting the recorded value by each strain gauge during testing.

Strain was further computed along straight paths through the discs using the Construction Path feature. These paths were set up to predict the strain at 50 points along the wheel radius, midway through its thickness[5]. The construction geometry path was set up to return the 'equivalent strain' at each point i.e. the scalar form of the strain at this point, removing the directional aspect of this quantity. Equation 3.1 is used in the ANSYS solver to calculate the equivalent strain at a point, ϵ_{eq}. Here, each of the ϵ_{xyz} terms represent the components of the strain tensor at that point with respect to the FE model coordinate system, and ν represents the Poisson ratio of the material. It should be noted that strain sensor measurements can only match the equivalent strain if the sensor is oriented in the absolute optimum direction relative to the target body. The failure to do so would result in the sensor

[5]Surface strain is the quantity of interest in these investigations, as this is what will be measured by the strain sensors. However, the strain going through the wheel midsection was used as a proxy here to streamline the data analysis process. Preliminary simulations revealed minimal differences between the strain inside the wheel's cross-section, and strain on its surface (0.5% on average) as it was a thin disc, so this was deemed a reasonable simplification.

failing to capture all the underlying strain in the discs[6].

$$\epsilon_{eq} = \left(\frac{1+\nu}{2}\right)^{\frac{1}{2}} \left[(\epsilon_{xx}-\epsilon_{yy})^2 + (\epsilon_{yy}-\epsilon_{zz})^2 + (\epsilon_{zz}-\epsilon_{xx})^2 + 6\left(\frac{\epsilon_{xy}^2+\epsilon_{yz}^2+\epsilon_{zx}^2}{2}\right)\right]^{\frac{1}{2}} \quad (3.1)$$

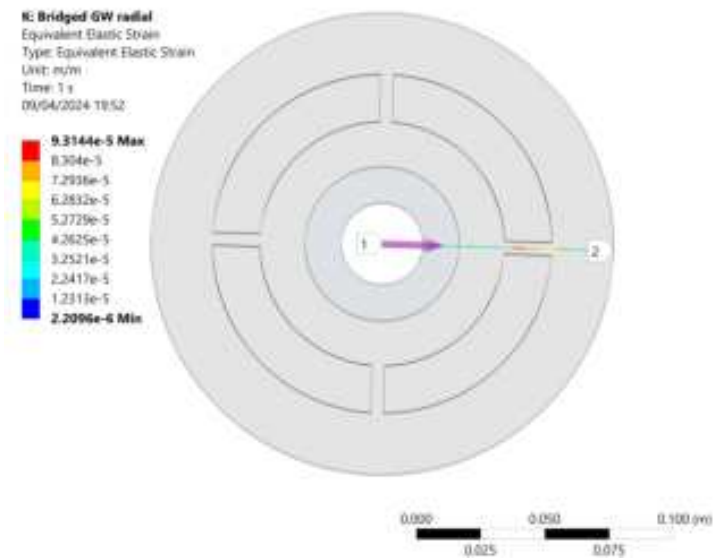

Figure 3.7: Equivalent strain plot generated with construction path feature.

3.5 Summary

Chapter 3 presented the experimental methodology and FE modelling approach used in this project. The requirement of reference measurements for FE model validation was highlighted, and a description was given of the mechanical testing procedures used to obtain these measurements.

The need to make key simplifications to the grinding wheel system for facilitating strain measurements in this project was also explained. The simplification and reduction of a grinding wheel in motion down to a disc under static loading was important here, as it allowed the creation of a system analogous to grinding conditions. This system involved the use of the in-plane torsion testing method for a first attempt at FE model validation in Chapter 4. The third simplification (reducing the disc geometry down to that of a beam under torsion) was then used in a follow-up experiment in Chapter 4. This simplification was conducted to create a simpler system which could be used to identify the sources of error arising in Chapter 4. Finally this, FE modelling was conducted in Chapter 6 for evaluation of the potential of embedded strain sensors for force measurement in grinding wheels.

[6]The scalar nature of equivalent strain meant that it was not suited to comparisons against strain gauge data- as the strain gauge results are highly dependant on direction. As such, it was used only for relative comparisons of disc and wheel geometries.

4 Simplified Disc Structure: Results and Discussion

Chapter 4 outlines a series of three experiments focusing on the in-plane torsion testing method. Several challenges were faced throughout this process, and each of the investigations served as an exploration of the issues identified in its predecessor. The first investigation involved subjecting the 5 mm thick simple disc to in-plane torsion. The second experiment replicated this process, but this time the 3 mm thick disc was used to better facilitate strain measurement. A third investigation was subsequently conducted, which involved varying the clamp position to measure the strain distribution throughout the wheel. Finally, FE model predictions were made for this third investigation, with the aim of conducting model validation.

4.1 5 mm Disc Tests

4.1.1 Approach

This investigation focused on in-plane torsion testing of a 5 mm thick disc, using the methodology outlined in Section 3.3. Four strain gauges were installed in a line on the disc's top surface, as seen in Figure 4.1, with clamps fixed to three points on its periphery. Stress (and therefore strain) concentrations were expected near the clamped position, based off similar examples in the literature [132], [133], so it was hoped that the three-clamp setup would facilitate high strain levels for accurate measurement. This was done to facilitate uniform strain throughout the wheel. A risk existed that using three clamps would over constrain disc deformation, thereby limiting strain, but it was deemed a worthwhile issue to investigate.

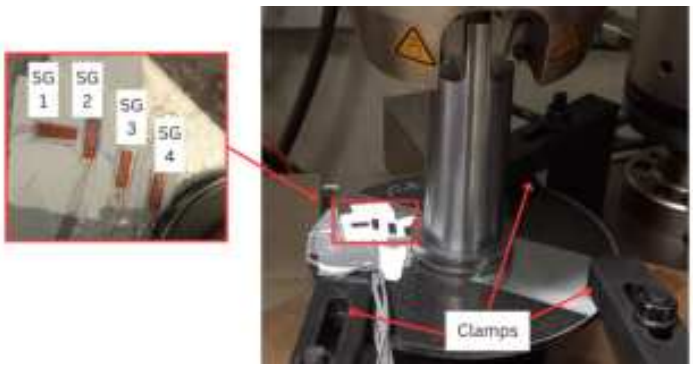

Figure 4.1: In-plane torsion testing of 5 mm disc.

4.1.2 Results

The strain measurements results are shown in Figure 4.2, which plots strain signal against time for the three loading tests. There is no clear separation between the loading and idle stages of each test here, even after applying 30 point averaging. There is also no clear strain separation between the 3 tests, as would be expected; the maximum strain levels were reached by the 20 Nm loading tests rather than the 30 Nm test as would be expected. These erratic strain gauge signals are not providing meaningful data, and it is not useful to calculate the average strain value for each of the tests.

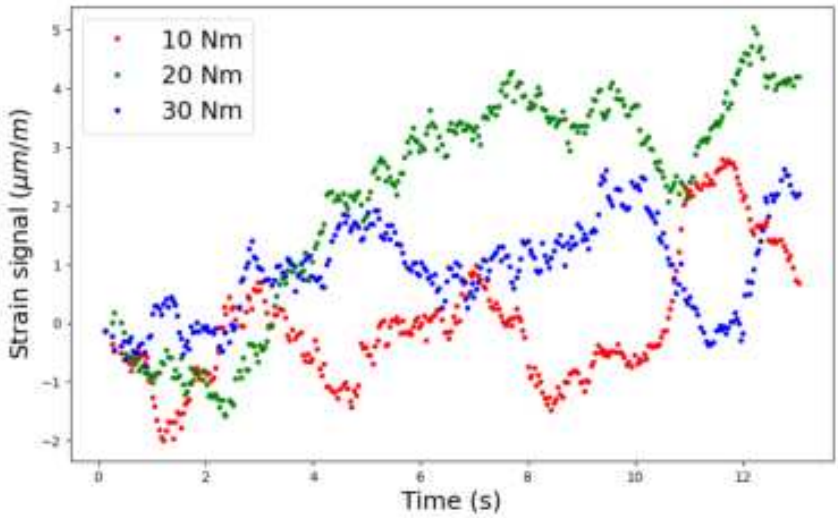

Figure 4.2: Signal from strain gauge installed on 5 mm disc (after applying 30 point averaging).

This behaviour was investigated with the FE model, which revealed that the strain experienced by this disc was too low for strain gauge detection (even at the maximum applied torque of 30 Nm). Predicted strain increases at the locations of the strain gauges were less than 6 $\mu m/m$- these would have been almost completely obscured by signal variations stemming from noise, explaining the poor results here.

The noise stems from variations in the Wheatstone bridge's excitation voltage, which was isolated in a standalone test. In this experiment, the data acquisition system was used to record the strain gauge signal for 5 minutes, without any load being applied to the gauge. This meant that all signal variances here would be caused solely by voltage fluctuations, allowing their behaviour to be isolated and quantified. The noise was found to introduce a mean error of ± 4 $\mu m/m$ into the signal, explaining why it was difficult to detect the strain in this experiment. Higher strain levels would be required to lessen the effects of noise in future experiments.

Two reasons were highlighted for the low strain levels in the disc here- overconstraint and excessive disc stiffness. The former was investigated by removing two of the three clamps

attached to the disc and visually observing the strain gauge signal under torsion in real time. This trial yielded no observable strain, so the disc was deemed too stiff to demonstrate measurable strain at the chosen torsion levels. A thinner disc would be trialled in Section 4.2 in the hope that it would provide less resistance to deformation, thereby better facilitating strain measurement.

4.2 3 mm Disc Tests

4.2.1 Approach

The in-plane torsion testing method was used again in this investigation, but here a 3 mm thick disc was used, in the expectation that its reduced thickness (and consequently, its lower stiffness) would produce more strain. If realised, the anticipated strain increase would enhance the signal-to-noise ratio, thus allowing disc strain measurement.

A rectangular rosette strain gauge was installed on the disc, as seen in Figure 4.3. This sensor was selected so that the distinct orientation of the gauge's three grids could be used to determine the primary strain direction. Only one clamp was fixed to the wheel here, in contrast to the three used in the previous experiment. This was attached at the wheel periphery, in close proximity to the rosette strain gauge.

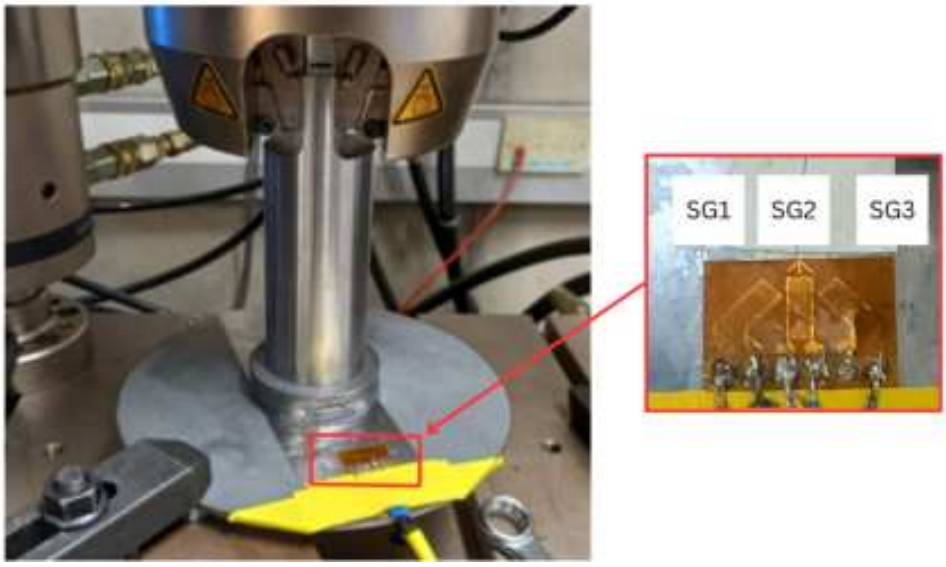

Figure 4.3: In-plane torsion testing on 3 mm disc.

4.2.2 Results

The reduction in disc thickness led to observable levels of strain in this investigation, raising it above the level of noise. This enabled a clear differentiation between the idle and loading stages in each test (see Figure 4.4), which allowed the strain to be measured at each load step. While noise remained a factor in the signal, its influence was lessened here. The strain gauge signal did not return exactly to zero after unloading which may have been due to hysteresis or noise in the system feeding into the 30 point moving average.

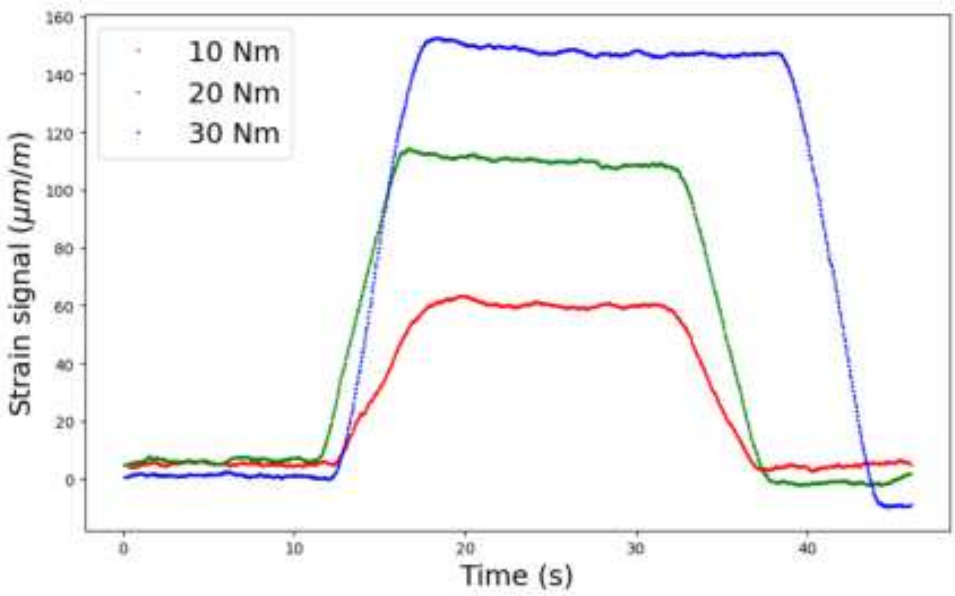

Figure 4.4: SG1 signal (after 30 point averaging).

The use of just one rosette strain gauge on the disc meant that only 3 strain gauge outputs were obtained at each torsion level. This resulted in a total of 9 strain readings across the load range, which was enough to investigate the effects of the disc thickness reduction, but not to fully validate the FE model. Validation of the FE model will be addressed with a dedicated investigation in Section 4.3.

4.3 FE Model Validation

4.3.1 Approach

The FE model strain prediction capabilities were evaluated in both qualitative and quantitative terms in this experiment. The former requires the model to successfully predicting the general disc strain patterns observed under loading. The latter is more difficult to achieve, as it involves accurately forecasting the absolute strain values at each of the sensor positions.

Ostensibly, measuring the strain patterns across the disc necessitates installing many strain

gauges which would be a costly and time consuming process. However, by varying the clamp position, one strain gauge could be used to measure the strain at a variety of different points in the strain pattern. This method was adopted here, where the rosette strain gauge alone was used to measure the strain in the 3 mm disc. Its three grids were labelled SG 1, SG 2, and SG 3, as is seen in Figure 4.5.

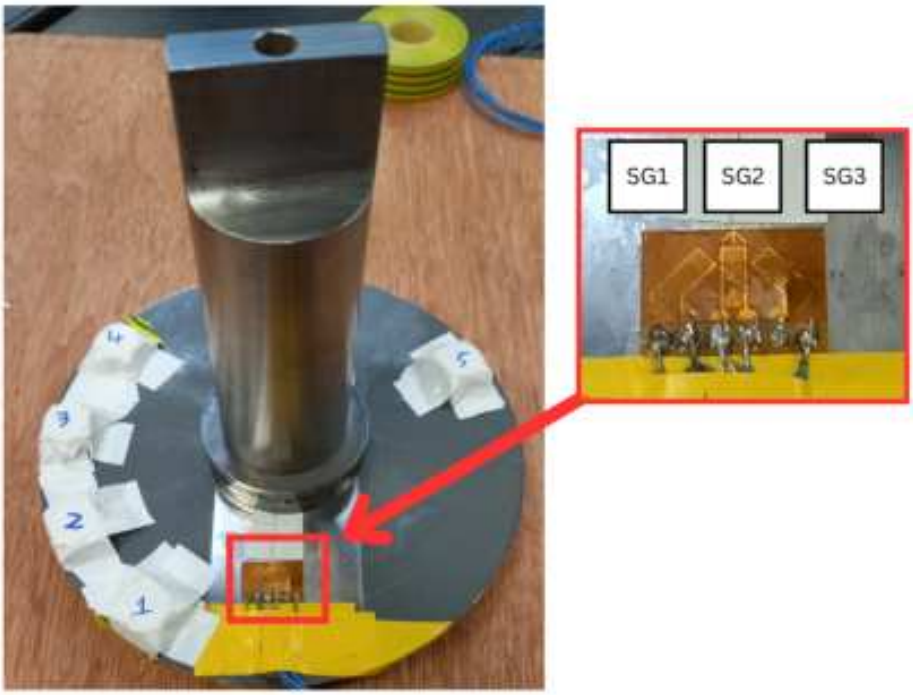

Figure 4.5: Strain gauge and clamp position labelling.

The clamp was fixed to the disc at 5 different positions in turn, with the strain being recorded at torsion levels of 10 Nm, 20 Nm, and 30 Nm for each clamp position. These positions were located such that they made angles of 30°, 60°, 90°, 120°, and 240° to the strain gauge positions about the vertical axis, numbered 1 to 5 in Figure 4.5[1]. Washers were glued to the disc surface at each of these positions before testing commenced, ensuring a consistent contact area between the clamp and disc which could be measured precisely and subsequently mirrored in the FE model.

4.3.2 Results

The strain measurements taken in this investigation were erratic, and no consistent trends were visible in the data. This can be seen in Figure 4.6, where no clear patterns are visible the strain measurements of SG 1 across the range of applied torsional moments. The same is true for the measurements obtained from SG 2 and SG 3.

[1]An ideal investigation here would include clamp positions ranging all the way from 0° to 360°, separated by smaller increments 15°. However, these tests were prohibitively time-consuming, so just 5 positions were tested.

The FE model predicted peak strain values to occur for SG 1 when the clamp was near the strain gauges, at Position 1 and Position 2 (corresponding to 30° and 60° in Figure 4.7). The strain gauge was then expected to record low strain values for Positions 3 to 5, due to the increasing distance from the clamp. However, this was not demonstrated in the experimental results, which displayed an apparently random distribution of strain values across the range of clamp positions, peaking at Positions 4 and 5- markedly different qualitative behaviour.

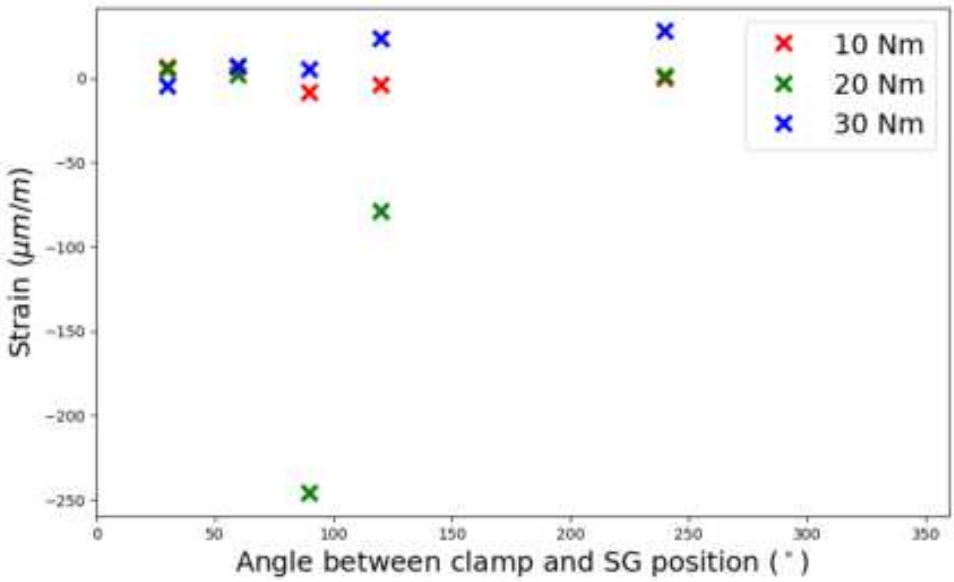

Figure 4.6: SG 1 results.

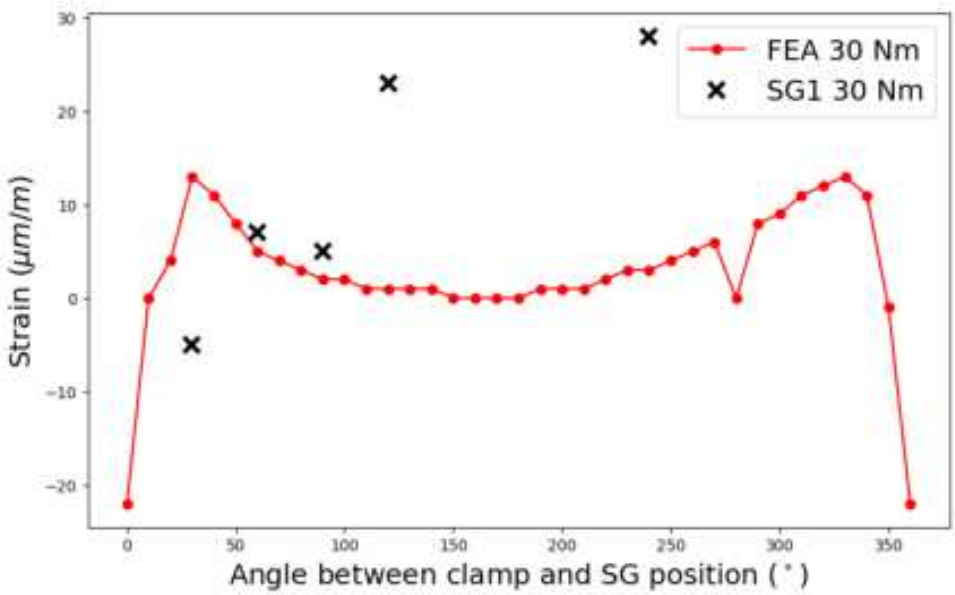

Figure 4.7: Comparison of SG1 results at 30 Nm torque to FE model.

The two approaches also differed substantially in quantitative terms, as average deviations of 3,350%, 200%, and -292%, being observed between the measured and predicted strain values for SG1, SG 2, and SG 3 across the entire load range.

Measurement error likely played a considerable role in the observed discrepancies, as evidenced by the absence of a clear and consistent strain trend across different levels of torsion. The strain gauge installation process was most likely a contributing factor here, as was confirmed with later strain gauge inspections under a microscope. An air bubble was observed beneath the rosette strain gauge carrier, indicating a sub-optimal strain gauge installation process which would have to be refined in further experiments.

The FE modelling approach represented another possible error source here. The model was still yet to be validated, and it was not known if errors were being made during its setup, or if it had a fundamental inability to accurately predict strain. Simpler experiments would have to be conducted to investigate this issue and to establish confidence in the model predictions.

4.4 Summary

This chapter focused on the torsion testing of a simplified disc structure to produce a static loading system producing torque loads and strains analogous to those observed in grinding systems.

The in-plane torsion test was conducted on a 5 mm thick disc, but this proved too stiff to produce observable levels of strain in the applied torque range. A 3 mm thick disc was tested in a subsequent investigation, producing greater levels of strain, and thus making strain analysis much more feasible.

The final experiment aimed to validate the FE model by comparing its predictions against actual strain measurements from various sensor positions around the disc. A single rosette strain gauge was used to measure strain at multiple points on a 3 mm disc by altering the clamp position, circumventing the need for numerous strain gauges, which are costly and time-consuming to install. This investigation did not yield the desired results, as the strain gauge measurements were erratic with little correlation to FE model predictions.

The strain gauge installation process emerged as a potential source of experimental error, so an adapted installation procedure was trialled in Chapter 5. Additionally, inaccuracies may have been present in the FE model, so Chapter 5 is also dedicated to investigating the strain prediction capabilities of the FE approach.

5 Simplified Beam Structure

Chapter 4 discussed the initial experiments conducted using the in-plane torsion testing approach, noting a poor correlation between predicted and observed strain readings. This was attributed to two primary factors: the method used for attaching strain gauges and inaccuracies present in the Finite Element (FE) model. Chapter 5 focuses on addressing these issues. Improvements were first made to the strain gauge application method to ensure a more effective strain transfer from the test object to the sensor. Bending strain was generated in the beams via static loading tests, with measurements being taken and analysed to determine the maximum achievable strain gauge accuracy. The FE model's capacity to accurately predict bending strain was also evaluated here.

A subsequent investigation was then conducted into the measurement of shear strain in a beam with strain gauges. It was hoped that this would facilitate an analysis of ANSYS software's shear strain capabilities. A final series of beam tests were then conducted, these evaluating the effects of unexpected beam deflection on the shear strain experiment. This behaviour could result in unintended bending strain, thereby affecting the strain gauge signals and potentially compromising the accuracy of shear strain measurements.

5.1 Disc to Beam Simplification

The work in this chapter is based on an additional simplification made to the grinding wheel analogy outlined in Chapter 3, with the disc geometry being reduced down to that of a rectangular beam under an applied load. If the beam is clamped at one end and a static load is applied to the other, the static load will mimic the torsional moment acting on the disc Therefore, it was expected that the beam would demonstrate comparable strain behaviour to a segment of the disc during torsion testing, as illustrated in Figure 5.1. This reduction allowed the strain to be analysed with simple bending theory.

The type of strain being measured varied depending on the surface which the strain gauge was located on. If positioned on the top or bottom faces under applied vertical loading, the gauge would experience bending strain. The gauge would experience shear strain if positioned on the sides of the beam. The beam orientation was varied in these experiments to allow the measurement of both shear and bending strain with the same strain gauges. When the beam was clamped along its width, the strain gauges experienced bending strain, as seen in Figure 5.2. The beam was then turned on its side to produce measurable shear strain, as demonstrated in Figure 5.1(b).

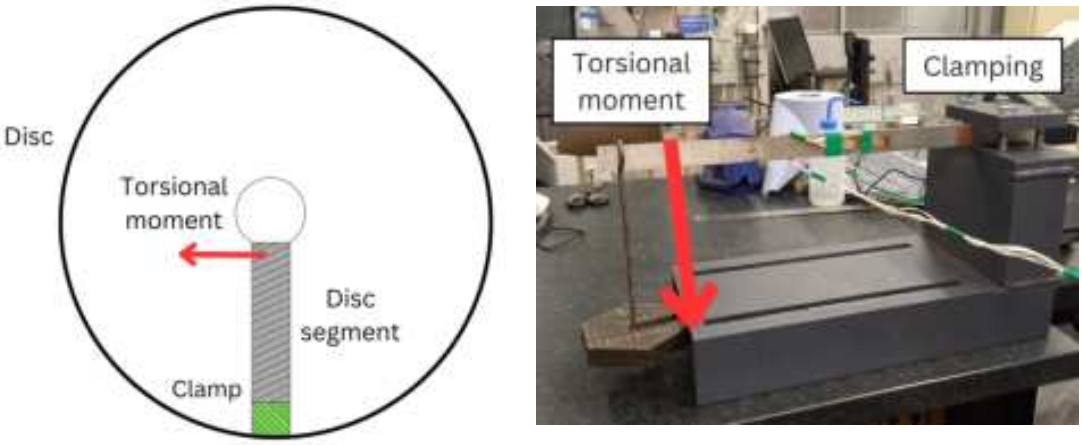

(a) (b)

Figure 5.1: a) Schematic diagram and b) practical application of the disc to beam simplification.

The grinding wheel/disc/beam analogy is continued with these orientations, where the bending strain demonstrated by the beam is akin to that observed in a disc or grinding wheel under axial loading. The beam shear strain is also comparable to that observed in a disc or grinding wheel, being induced by torsional moments, tangential forces, or normal forces in these situations.

5.2 Refined Strain Gauge Application Process

A refined strain gauge application process was used to enhance the adhesion (and therefore the strain transfer) between the sensor and the test object. This process included three additional steps in surface preparation: cleaning with a conditioner acid followed by two neutraliser solutions. The conditioner acid was used to eliminate oxides from the target surface, the first neutralizer to remove the conditioner, and the third to leave a neutral pH on the target surface. The strain gauge was then immediately applied to prevent the formation of a new oxide layer that could undermine the procedure. M bond 610 adhesive from Micro Measurements, a two-component, solvent-thinned, epoxy-phenolic adhesive specifically designed for strain gauge applications, was used to affix the strain gauge to the surface.

5.3 Bending Strain Investigation

5.3.1 Approach

A test rig was set up, with a high carbon steel beam clamped at one end and subjected to static loads at the other as shown in Figure 5.2. The strain gauges were used to measure the resulting bending strain in the beam, a straightforward application allowing their maximum achievable accuracy to be determined. The static loads were applied using steel weights ranging from 50 g to 900 g (i.e. from 0.4905 N to 8.829 N), producing bending strain in the beam. The load was applied in a total of 9 steps with a 10 second holding period at each load step[1].

A rectangular rosette and tee strain gauge were both installed on the beam using the refined installation process. These are shown in Figure 5.2, where the rosette strain gauge grids are labelled 1, 2, and 3, and the tee grids are labelled 4 and 5. SG 2 and SG 5 are aligned in parallel with the beam neutral axis, hence they are referred to as 'axial gauges' here. The use of the rosette strain gauge allowed calculation primary strain direction[2] to be calculated. This was done according to Equation 5.1, where ϵ_1 represents the strain recorded with SG 1 at a given load, with ϵ_2 and ϵ_3 representing the corresponding measurements from SG 2 and SG 3, respectively.

$$\theta = \frac{1}{2}\tan^{-1}\left(\frac{\epsilon_1 - 2\epsilon_2 + \epsilon_3}{\epsilon_1 - \epsilon_3}\right) \tag{5.1}$$

A Kistler 9232A piezoelectric surface strain sensor was also bolted onto the beam (see Figure 5.2) and connected to a Kistler Type 5015 charge meter. This sensor would serve as a benchmark for comparison here, indicating what practical limit for strain gauge measurement was on the beam. The charge meter was adjusted to provide a sensor sensitivity of 300 pC per $\mu m/m$ and to offer a display resolution of 1 $\mu m/m$.

A FE simulation was developed to mirror the test setup, with remote forces applied to the beam end to replicate the static loads. A higher order tetrahedral mesh was used again here, this time with a mesh size of 1.5 mm (determined with another mesh independence study), as shown in Figure 5.3. AISI 1340 carbon steel material properties were assigned to the beam model. The strain gauges and Kistler sensor were then modelled with the shell element method (Section 3.4.4), and fixed geometry was assigned to the beam at the clamping sites to reflect the experimental conditions.

[1]This loading pattern was only applied once due to time constraints. It represents a deviation from standard scientific practice in which experiments are typically conducted three times to ensure repeatability.

[2]The direction which yields the highest strain readings at a given point. This is calculated relative to the beam neutral axis here.

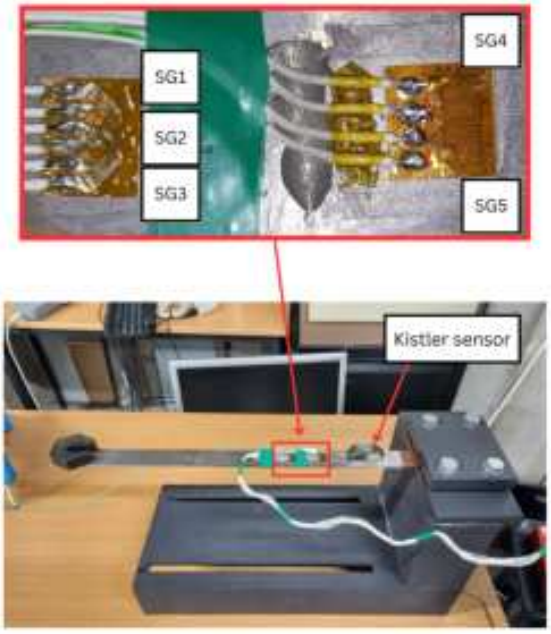

Figure 5.2: Experimental setup for bending strain tests.

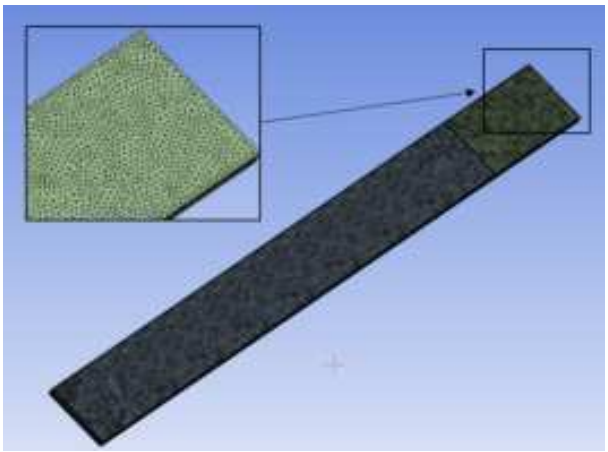

Figure 5.3: FE beam model mesh.

Simple bending theory was applied to analytically calculate the strain in the beam, providing a theoretical upper limit for the measurable values. Equation 5.2 was used to calculate the strain at each of the axial gauge positions in this manner [137]. Here, L_1 represents the distance between the sensor and the beam end, t represents the beam thickness, F represents the force applied to the beam end, and I the 2nd Moment of Area of the beam. E represents the Young's Modulus of the beam; this was taken here to be 2×10^{11}, matching the material property assigned in the simulations.

$$\epsilon = \frac{FL_1 t}{2EI} \tag{5.2}$$

5.3.2 Results

The Kistler sensor and strain gauges were installed at different locations on the beams, so their measured strain values could not be directly compared on the same charts[3]. Instead, each sensor was compared via their relative performances against the FE model and analytical strain predictions.

The Kistler sensor exhibited excellent linearity throughout the range of loads (R^2=0.999), as seen in Figure 5.4. This trend is consistent with the analytical and FE model predictions, both of which simulated a direct proportionality between beam load and strain. However, the sensor registered significantly less strain than anticipated, averaging 68% and 70% less strain than the analytical and FE methods, respectively.

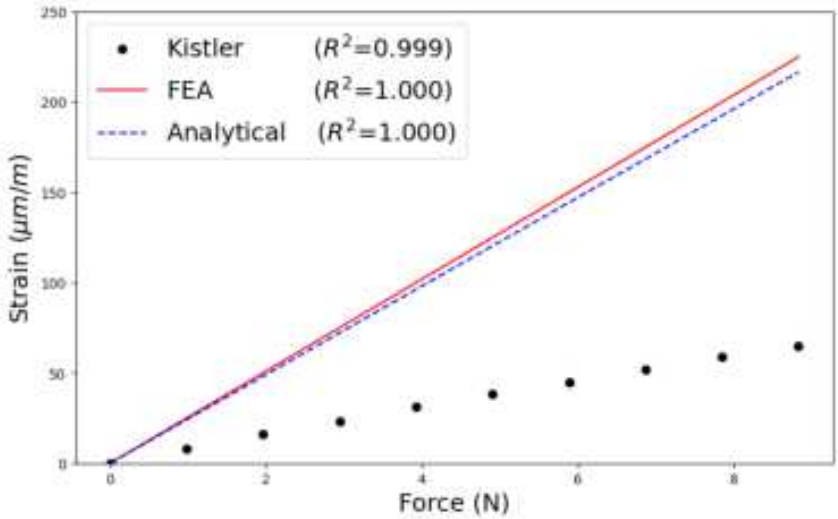

Figure 5.4: Kistler sensor bending strain measurements.

SG 2 and SG 5 also demonstrated good linearity, achieving R^2 values of 0.993 and 0.997 respectively. Small strain gauge signal fluctuations were present below a threshold of 30 $\mu m/m$, sightly affecting the linearity up to this point. However, the fluctuations diminished above the 30 $\mu m/m$ threshold, after which the effects of noise became less significant.

The measurements from SG 5 closely matched the FE model and analytical strain predictions, agreeing to within 6% of the predicted values for all load steps (see Figure 5.5). SG 2 demonstrated similar behaviour to the Kistler in that, on average, its results were 68% and 70% lower than its analytical and FE method equivalents. However, the data from SG 3 reveals an important trend. This sensor, predicted to have low strain values due to its non-axial alignment, in fact recorded strains which were in line with the FE predictions for SG 2. This sensor's measurements agreed to within 4% of the analytical and FE predictions for SG 2 at all load steps above 1 N, demonstrating a high degree of accuracy.

[3]An ideal setup would have placed both types of sensors at identical positions on two matching beams; however, constraints related to the project's budget and timeline precluded this arrangement.

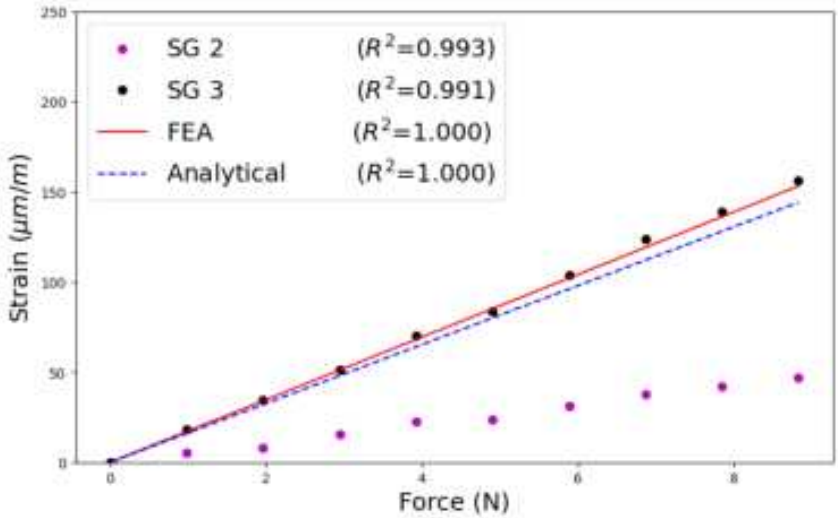

Figure 5.5: SG 2 and SG 3 bending strain measurements.

The data from SG 1, SG 2, and SG 3 were subsequently used to calculate the primary strain angle, and this revealed the cause of the unexpected behaviour. The experimental values showed that the primary strain was aligned with SG 3 (see Table 5.1), rather than being oriented along the beam neutral axis as was predicted. SG 3 made an angle of 45 ° with the neutral axis, and the primary strain angle agreed to within 6.5 ° of this orientation at all load levels. This also explains why the Kistler sensor recorded low strain values, as it was not oriented in the correct direction to capture the primary strain. This behaviour indicated a degree of asymmetry in either the beam load application, or the beam's response to loading. The load may potentially have been applied "out-of-plane" i.e. not in the plane extending vertically from the beam's neutral axis, or it may have been bending outside of this plane. This asymmetry would be a key factor in the investigations to follow.

Load (N)	**SG 1 strain ($\mu m/m$)**	**SG 2 strain ($\mu m/m$)**	**SG 3 strain ($\mu m/m$)**	**Angle to neutral axis (degrees)**
0.981	-3	5	18	38.56°
1.962	-11	8	35	40.46°
2.943	-15	16	52	42.80°
3.924	-21	22	70	43.45°
4.905	-25	24	84	42.18°
5.886	-32	31	104	43.09°
6.867	-36	38	124	42.66°
7.848	-42	42	139	43.06°
8.829	-47	47	156	42.78°

Table 5.1: Primary strain direction calculated from experimental results.

In summary, the strain gauges were successfully used to measure the strain in this experiment. These sensors provided accurate results which agreed much more closely with the FE model and analytical strain calculations than those of the Kistler sensor. Confidence was established in their measurements, validating the accuracy of the refined strain gauge application method.

5.4 Shear Strain Experiment

5.4.1 Approach

The test rig was setup as outlined in Section 5.3.1, but with a slight alteration. Figure 5.1(b) shows how the beam was clamped on its side in this iteration, leaving the strain gauges on the beam face experiencing shear strain this time[4]. Weights were attached to a hook and hung from the top surface of the beam to generate the strain, these again varying from 50 g to 900 g (0.4905 N to 8.829 N)[5]. The FE model was adapted to account for the change in beam orientation and was run again to predict the shear strain at the sensor positions. The analytical shear strain was calculated at the axial strain gauge positions, this time using Equation 5.3 [137]. Here, y represents the distance of the strain gauge from the beam neutral axis.

$$\epsilon = \frac{FL_1 y}{EI} \tag{5.3}$$

5.4.2 Results

The measurements taken by SG 2, SG 3, and SG 4 in this investigation were inconsistent, failing to demonstrate a clear trend across the load range. This can be seen in Figure 5.6, where the R^2 values indicate little to no correlation between strain measurements (0.392, 0.142, and 0.657 respectively). In contrast, SG 1 and SG 5 demonstrated good linearity, with their respective plots giving R^2 values of 0.955 and 0.945.

This qualitative behaviour is reflected in the FE model, which anticipated a linear escalation in strain with added load again. However, SG 1 recorded compressive strain across the entire load range which contradicts the FE model's predictions of tensile strain throughout. SG 5 stands as the only sensor with measurements which match the general trend predicted of it by the model, and even then, its values are 61% lower than expected on average.

Overall, there is little correlation between the FE model and experimental results for this

[4]The Kistler was excluded from the shear strain tests, as it is can only measure linear (bending) strain.

[5]This loading pattern was only applied once due to time constraints. It represents a deviation from standard scientific practice in which experiments are typically conducted three times to ensure repeatability.

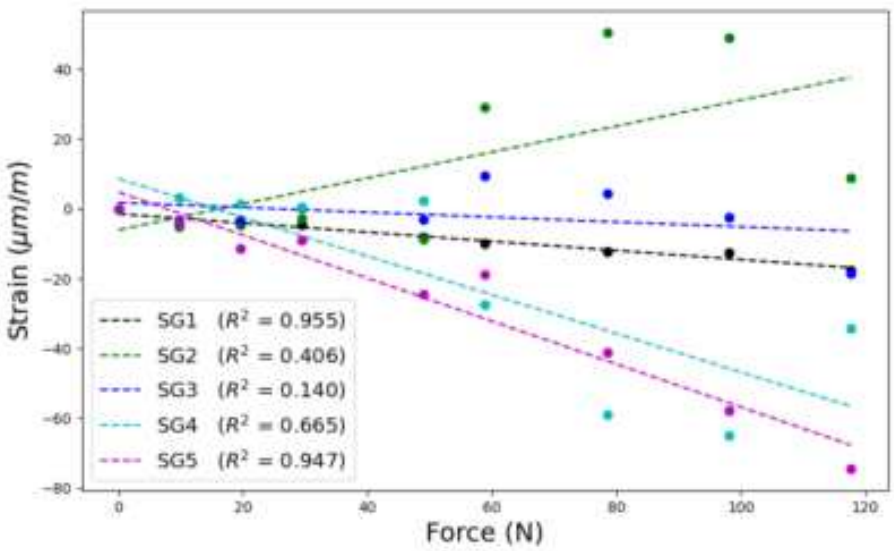

Figure 5.6: Shear strain values recorded by the 5 strain gauges.

investigation. Of these two approaches, error in the experimental approach was highlighted as the main cause of this disparity, due to the degree of inconsistency in the strain gauge results. The work conducted in Section 5.3 already established a confidence in the strain gauge measurements, so this was ruled out as a source of error. However, a visual examination of the experimental setup revealed that out-of-plane deflection occurred when vertical load was applied. This deviation could have influenced the study by adding unanticipated bending strain to the beam. It is possible that this bending strain was reflected in the strain gauge readings, which may account for the irregular shear strain figures observed. The impact of this behaviour was further explored and quantified in the investigation detailed in Section 5.5.

5.5 Beam Deflection Investigation

5.5.1 Approach

The experimental apparatus from 5.4.1 was replicated in this experiment, but this time a digital dial indicator was set up beside the beam to record unintended out-of-plane behaviour. The digital dial indicator was fixed with its probe in contact with the beam (as seen in Figure 5.7), such that any out-of-plane deflection would be captured.

The device output was zeroed while the beam was unloaded before each set of tests. Weights were applied via a hook to generate shear strain in the beam, these again applied in 9 load steps varying from 50 g to 900 g (0.4905 N to 8.829 N). The probe displacement was recorded for each load step and was then used to determine if bending strain was present in the beam. The experiment was conducted 3 times, removing the beam, and clamping it

Figure 5.7: Digital dial indicator for detecting out-of-plane beam deflection.

again between each repetition. This would highlight if small variations in beam positioning were causing the beam to bend in an unexpected manner i.e. away from its neutral axis. The beam was aligned at exactly 90° to the clamp using a tee-square and metre ruler to minimise this off-axis bending. Strain gauge readings were not taken during this investigation as measurements of beam deflection alone would allow the bending strain to be calculated. Finally, the deflection measurements were factored into Equation 5.4 to quantify the bending strain at the position of each of the strain gauges. Here, δ represents horizontal beam deflection, with L1 and L2 representing the distances from the strain gauge position to the end of the beam, and the beam length, respectively [137].

$$\epsilon = \frac{3\delta L_1 t}{2L_2^3} \tag{5.4}$$

5.5.2 Results

A significant amount of out-of-plane beam deflection was observed under static loading in all three tests, as shown in Figure 5.8. In general the beam deflection displayed a linear relationship with applied load, with R_2 values of 0.902 for Test 1 and 0.979 for Test 2. Less correlation was displayed between deflection and applied load for Test 3.

A peak deflection of 2.2 mm was recorded in Test 2, this corresponding to a bending strain of 44 $\mu m/m$ when factored into Equation 5.4. This is shown in Table 5.2, where positive and negative values indicate tensile and compressive strain, respectively.

Significant variability exists in the recorded deflection figures, with 2.65 mm separating the minimum and maximum values. The direction of deflection also varied from test to test, showing positive values in two cases and negative in the other. This volatility makes it difficult to quantify and/or predict, so attempts to isolate the bending beam strain from shear strain would be extremely difficult.

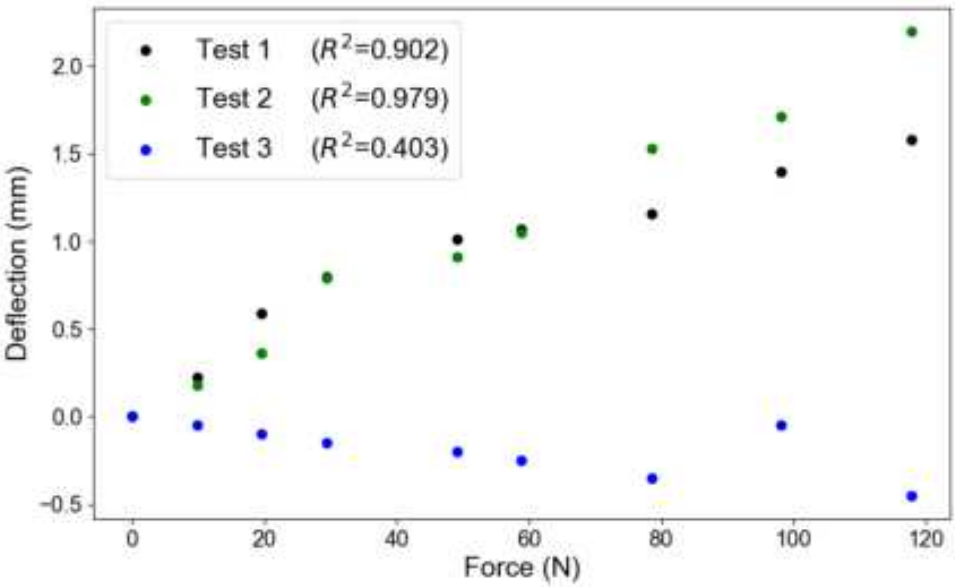

Figure 5.8: Out-of-plane beam deflection under shear loading.

Test	Max deflection (mm)	Bending strain ($\mu m/m$)
1	1.58	31.6
2	2.2	44
3	-0.45	-9

Table 5.2: Maximum out-of-plane deflections and corresponding bending strains.

5.6 Summary

This chapter investigates the main potential sources of error from Chapter 4, using an additional simplification to the grinding wheel/disc analogy (reducing these geometries to a beam under torsion).

The first investigation trialled a refined strain gauge application method and evaluated the resulting strain gauge accuracy with the measurement of bending strain in a cantilever beam. The method was deemed a success, as the strain gauges achieved high levels of accuracy here. The FE model strain prediction capabilities were validated here, agreeing with strain gauge values to within 6% when the effects of misaligned loading were considered.

A second investigation was conducted to determine the shear strain prediction capabilities of the FE model, based around strain measurement in a cantilever beam in a slightly altered setup. The measurements obtained were extremely inconsistent, which highlighted the possibility of error due to out-of-plane beam deflections.

A third investigation was then conducted to investigate this issue, where beam deflections of up to 2.2 mm were recorded under shear loading. Calculations indicated that this was

introducing significant amounts of bending strain into the strain gauge signal. This crucial finding may explain why such poor results were obtained in the experiments detailed in Chapter 4, as disc deflections (and thus bending strain) may have been at fault for the erratic strain measurements. This observation bears similarity to a comparable project by Grant [138], where out-of-plane forces also lead to large deviations between FE model predictions and strain gauge results. Future work could include the addition of guides to prevent the occurrence of out-of-plane deflection.

6 Sensor Potential Evaluation

This chapter uses the FE modelling approach detailed in Chapter 3 to evaluate whether embedded strain sensors can be for force measurement in grinding wheels. A conventional grinding wheel design was first evaluated as a potential location for embedded strain sensors, evaluating its strain sensitivity with respect to the three components of grinding force. A number of modified designs were then assessed, in the expectation that the modifications would enhance the sensors' force measurement capabilities.

6.1 FE Modelling Approach

The FE model was adapted to match the geometry of the conventional grinding wheel as initially described in Section 3.3.1, characterized by a maximum thickness of 13 mm and a minimum thickness of 5 mm at the bottom of the groove features (ref Figure 6.1(a)). A flat disc was created as a simplified version of this (Figure 6.1(b)), along with three other modified geometries engineered to potentially demonstrate higher ratios of shear strain to bending strain.

The third design (seen in Figure 6.1(c)) is referred to as the 'thinned' design, as deeper grooves were cut into this design to reduce its minimum thickness to 2.5 mm. The fourth design adapted a disc to incorporate 'shear bridges' as described by Brosius et al. [127], in addition to the grooves found in the conventional grinding wheel design. The aim was that the grooves would facilitate higher levels of shear strain, while the radially aligned bridges, or thicker sections of the disc, would resist bending strain. This geometry is referred to here as the 'bridge' design and can be seen in Figure 6.1(d).

Six slots were cut the whole way through the wheel in the final design, shown in Figure 6.1(e) and referred to here as the 'slotted disc'. This design is a simplified version of a design for optimised torque measurement which was proposed in a white paper by Transense [139]. Shear bridges were formed here again after the slots had been removed, and it was expected that these would exhibit elevated strain levels.

The conventional grinding wheel and simple disc designs were meshed using a uniform element size of 1 mm, which had previously been determined the optimal mesh size for these straightforward geometries (refer to Section 3.4.2). This same mesh size was applied to the other designs as well; however, stage 1 selective mesh refinement was applied to select locations in each of these to enhance model accuracy and resolution. The mesh in the thinned disc was refined below the grooved features to guarantee that the model maintained a minimum thickness of at least three elements at all points. In the case of the bridges

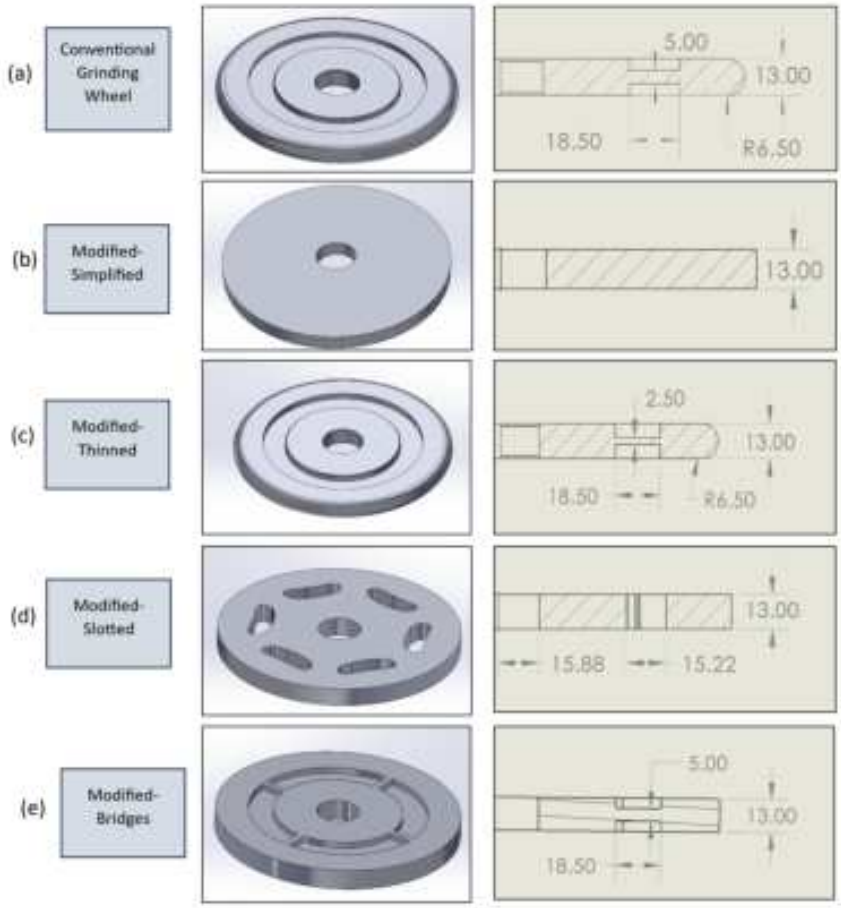

Figure 6.1: Conventional grinding wheel and optimised designs for enhanced strain sensitivity.

design, refinement was conducted in the shear bridge areas to ensure detailed stress and strain analysis in these critical sections. Finally, the mesh refinement for the slotted disc was focused on the slot edges to accurately capture the stress concentrations and deformations in these areas[1].

Remote force loads of magnitude 40 N were applied to a specific point on the exterior of each disc, as seen in Figure 6.2. This force magnitude, an arbitrary choice within the typical range of the three force components shown in Table 2.1, was imposed sequentially as axial, normal, and tangential loads. The washer-disc contact areas (blue in Figure 6.2) were then secured with fixed geometry constraints (red) to counteract these applied forces. Consistency across simulations was maintained by assigning the same material to each model (AISI 1340 carbon steel).

[1]See Appendix A2 for graphics of the discussed meshes.

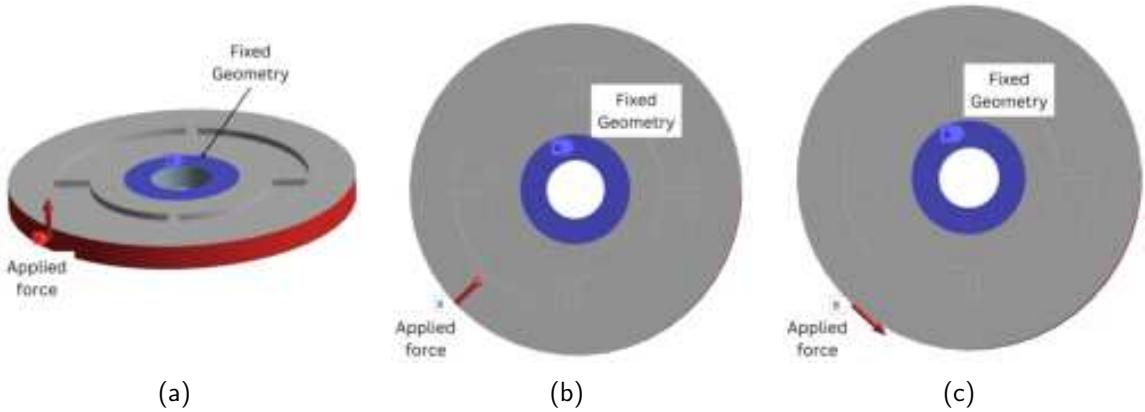

Figure 6.2: Boundary conditions for (a) axial (b) normal (c) tangential loading simulations.

The strain predictions for each of the designs were subsequently obtained using a construction path feature, as outlined in 3.4.5. The strain path was set up close to the point of force application as the highest strain values were expected near this point[2]. The equivalent strain was calculated at 47 points along the construction path, this path being shown in Figure 6.3(b).

For analysis purposes, names were assigned to three regions in the discs and wheels, these being labelled A, B, and C (as seen in Figure 6.3(a)). These regions were separated according to radial distance, with Region A denoting the volume inside a radius of 47.5 mm, Region C denoting that outside a radius of 66 mm and Region B denoting the volume between these two regions.

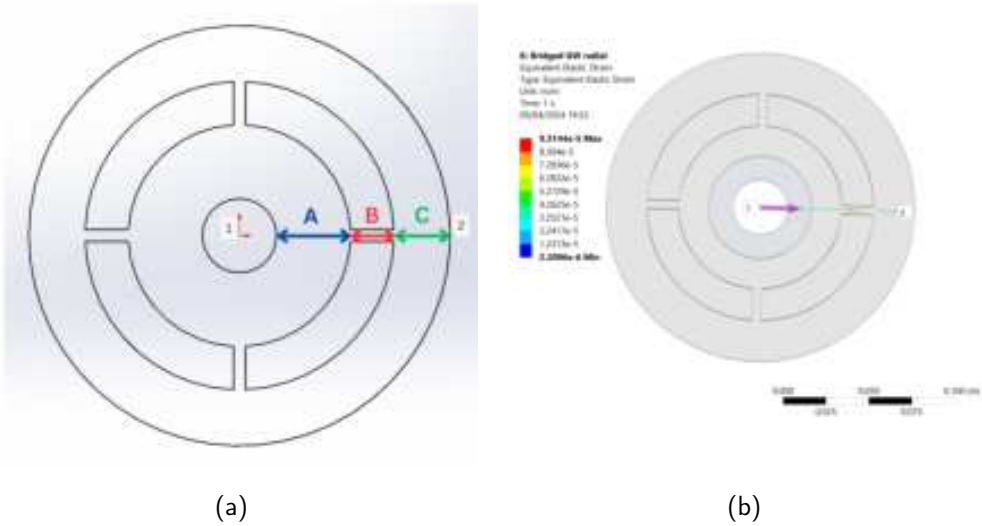

Figure 6.3: (a) Wheel region labelling and (b) equivalent strain plot for bridges design.

[2]The strain path was set up along a wheel radius here, with start and end points located at the wheel centre and wheel circumference, respectively. The strain path end point was located 45° away from the point of force application here.

6.2 Results and Discussion

6.2.1 Axial Loading

The strain distributions throughout the wheel and disc designs under applied axial loading are shown in Figure 6.4. Most of the designs showed the lowest strain values towards their exterior (Region C). Strain values were slightly higher near the centre at the washer contact area (Region A), with peak strain values predominantly occurring at Region B. These peaks suggest strain concentrations at points of reduced wheel thickness for both the conventional grinding wheel and the thinned grinding wheel. Strain concentrations were also observed in the 'shear bridges' of the bridges design and the slotted disc. The strain typically decreased with increasing radial distance where these features were absent.

The simple disc, although lacking strain peaks at Region B, otherwise exhibited behaviour closely mirroring that of the conventional grinding wheel here. Meanwhile, the slotted disc displayed minor deviations from the strain behaviour exhibited by the other designs at Region A. These deviations are not considered relevant here. The thinned grinding wheel is seen here to be most sensitive to strain under applied axial loading, followed by the slotted disc, then the conventional grinding wheel.

The strain levels observed under this type of loading were low, but measurable. The average strain values observed in each of the discs across the most sensitive region, Region B, ranged from 4.8 to 17.6 $\mu m/m$. This level of strain is observable with strain gauges, although noise may affect accuracy at this level.

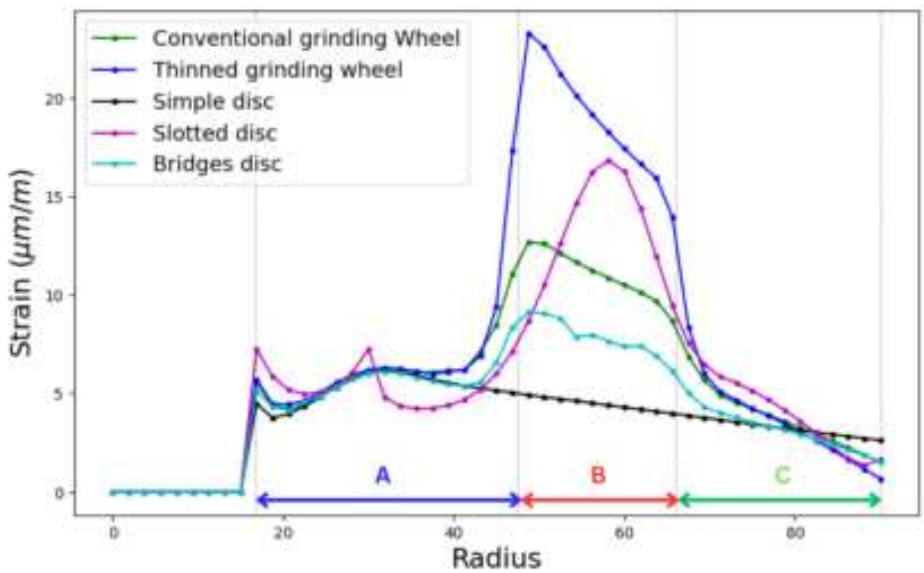

Figure 6.4: Bending strain distributions under applied axial force.

6.2.2 Tangential Loading

The strain distributions under applied tangential forces are shown in Figure 6.5. Extremely low strain levels were predicted under this type of loading, with a maximum strain value of 1.2 $\mu m/m$ predicted across all 5 wheel designs. The lowest strain values are observed in Region C, with peak strain predicted in area B for the conventional grinding wheel, thinned grinding wheel, and bridges designs. The strain is seen to reduce with increasing radial distance again here, in the absence of areas of features which lower the disc thickness. The slotted disc demonstrates a unique strain response here, in that its peak strain is predicted to occur in Region A. The increased level of strain is only observed over a small length of the disc radius, indicating that the strain concentration is highly localised. This suggests that material removal from Region B shifts the strain focus to Region A, a point of interest for design optimization. This strain pattern, especially the localized peak at Region A, presents challenges for detection with embedded strain sensors due to the significant variations over a small area. Excluding this strain peak from consideration, the thinned grinding wheel emerges as the design most responsive to strain from tangential forces, followed by the conventional grinding wheel.

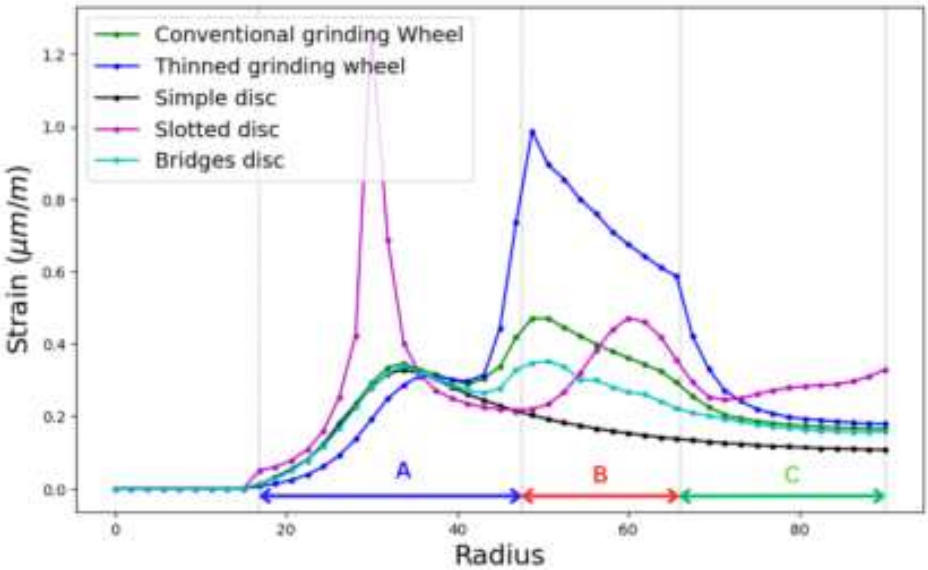

Figure 6.5: Shear strain distributions under applied tangential force.

6.2.3 Normal Loading

The strain distributions under applied normal forces are illustrated in Figure 6.6. Very low strain values were predicted under this type of loading, with the peak value given as 0.6 $\mu m/m$. Once more, the lowest strain values were observed in Region C, while strain peaks occurred in Region B for the grinding wheel, thinned grinding wheel, bridges, and slotted disc designs. Notably, the slotted disc again displayed an additional, highly localized strain peak

in Region A. In this scenario, the slotted disc showed the highest sensitivity to applied normal forces, followed by the thinned grinding wheel and the conventional grinding wheel.

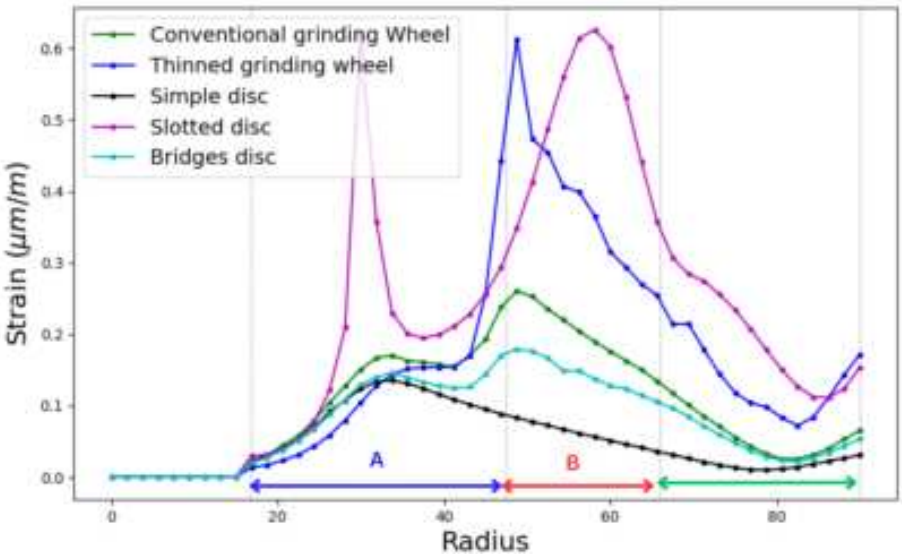

Figure 6.6: Shear strain distributions under applied normal force.

6.3 Force Response Comparison

Far greater strain magnitudes were observed under axial loading compared to tangential or normal loading, as illustrated in Figure 6.7, indicating the grinding wheel's significantly higher tendency to exhibit bending strain over shear strain. This pattern holds true across all five wheel/disc designs, as detailed in Table 6.1. Despite attempts to optimize the discs for enhanced shear strain, it was noted that these modifications did not increase shear strain without also escalating bending strain. Each of the designs are concluded to be much more sensitive to axial loading than tangential or normal loading. This observation further supports the hypothesis that the unsatisfactory results from in-plane torsion testing were due to bending strains caused by out-of-plane moments.

Force component	**Conventional grinding wheel** ($\mu m/m$)	**Thinned design** ($\mu m/m$)	**Simple disc** ($\mu m/m$)	**Slotted design** ($\mu m/m$)	**Bridges design** ($\mu m/m$)
F_A (bending)	10.8	17.6	4.7	11.4	7.8
F_N (shear)	0.2	0.4	0.1	0.4	0.2
F_T (shear)	0.4	0.7	0.2	0.3	0.3

Table 6.1: Comparison of average strains across Region B.

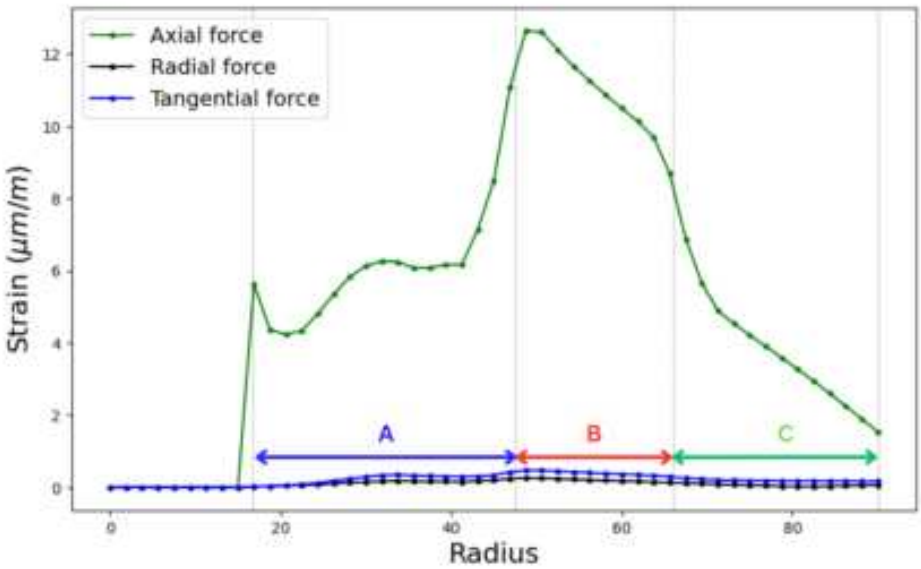

Figure 6.7: Strain distributions in conventional grinding wheel.

6.3.1 Embedded Sensor Potential: Conventional Grinding Wheel

The FE model results presented in Section 6.2 indicate strong potential for axial force measurement in a conventional grinding wheel. The typical axial load of 40 N was predicted to cause an average strain of 10.8 $\mu m/m$ across Region B in a conventional grinding wheel design, which demonstrates potential for SAW and MR sensor applications. The resolution provided by each of these sensors (0.2 $\mu m/m$ and 1 $\mu m/m$, respectively) is much smaller than the strain values which they are monitoring here, so it can be concluded that axial grinding forces may be measured using sensors embedded directly on a conventional grinding wheel.

The FE model results also suggested that very low strain levels would be generated in Region B of a conventional grinding wheel under applied normal and tangential forces (0.2 $\mu m/m$ and 0.4 $\mu m/m$, respectively). These figures are smaller than the MR sensor resolution, indicating that MR sensors would not be capable of detecting strain at the current level of applied force. Thus, it is concluded that MR sensors do not have potential for strain measurement in conventional grinding wheel designs. The SAW sensor would likely be capable of strain measurement at this force level, but may fail to detect force changes if the load drops below 40 N. An additional consideration in this evaluation was the higher sensitivity of the grinding wheel design to axial loading than to tangential and normal loading. Even if shear strains were present at a level that was detectable by the SAW sensors, their measurements could be compromised by axial loads acting on the wheel (as was demonstrated in Chapter 4). Therefore, it was concluded that SAW sensors demonstrate very limited potential for embedded measurement of tangential and normal forces.

6.3.2 Embedded Sensor Potential: Optimised Designs

The conventional grinding wheel design has been deemed suitable for embedded strain sensors to measure axial forces, though it falls short for measurement of tangential or normal grinding forces. Tangential and normal forces do not occur in levels sufficient to generate measurable strain across the entire range of typical grinding forces, and they generate much less strain in the wheel than similar levels of applied axial forces. These limitations extend to the optimized designs as well, where bending strain continues to predominate in the strain predictions. Although these designs show a slight improvement in the ratio of peak normal strain to peak shear strain, the enhancement is not sufficient to allow for effective shear strain measurement with embedded sensors.

Two of the designs (the thinned grinding wheel and the slotted disc), showed potential for increasing the levels of bending strain in the wheel, with peak strain values that were 83% and 32% higher. However, this increased sensitivity has its drawbacks; it renders the designs more prone to deflections, which could negatively impact the accuracy of the grinding process.

The dilemma between enhancing strain sensitivity and maintaining system accuracy through use of a sufficiently stiff grinding wheel does not have a universal solution. Instead, it must be assessed for each specific application, so evaluations of the sensitivity necessary to measure these designs are not straightforward. These must be conducted on a case by case basis to strike the correct balance between enhanced sensitivity and potential reductions in process accuracy.

6.4 Summary

This chapter explored the use of FE modeling to assess the potential of embedded sensors for force measurement in grinding wheels, evaluating five different designs: a simple disc, a conventional grinding wheel, and three modified versions aimed at improving shear strain detection. The analysis quantified their sensitivity to axial, tangential, and normal loading, finding that only axial loading produced high levels of strain responses under typical grinding conditions.

The optimised designs demonstrated capabilities for enhancing axial force measurement, but they could not produce enough shear strain to facilitate reliable tangential or normal force measurements. Therefore, it was concluded that embedded strain sensors have strong potential for axial force measurement in grinding wheels, but potential is limited for tangential or normal force measurement with this method.

7 Conclusion

This project used a combined experimental and Finite Element (FE) modelling approach to investigate strain in grinding wheels, and to understand if embedded strain sensors had the potential to measure the forces experienced by a grinding wheel in operation.

Several practical simplifications were made to reduce a moving grinding wheel to a static loading setup, in which reference strain measurements were taken for comparison against the FE model.

Chapter 4 details how the in-plane torsion testing setup was trialled for 5 mm thick and 3 mm thick discs.

- Experimental results for the 5 mm disc tests produced erratic signals which were within the noise band of the sensor. This suggests low levels of strain in the disc under the applied loads of 10 Nm, 20 Nm, and 30 Nm.
- The experimental results for the thinner 3 mm disc revealed observable levels of strain. An increase in strain levels was observed with increasing torque, as was expected.
- However, no clear correlation was found between the absolute values from these experimental results and finite element model predictions. The strain gauge-disc adhesion was highlighted as a potential error source, as were potential simulation errors.

Chapter 5 represented an investigation into the poor experimental-FE correlation. Further simplified experimental tests involving simple beam bending and shear beam bending tests were conducted, and the strain gauge application method was refined.

- Good correlation was observed between experimental, analytical, and FE model results for the simple bending experiment, establishing confidence in the FE model strain prediction capabilities.
- Poor correlation was observed between predicted and measured strain values in the shear bending test. The beam was seen to deflect horizontally under loading, with out-of-plane behaviour identified as a possible error source.
- An additional experiment measuring out-of-plane deflection was conducted, which found horizontal deflection to be a significant factor. It explained the poor correlation between FE model and experimental results, as unexpected bending strain had been introduced into the shear strain measurements.

Chapter 6 investigated the sensitivities of traditional and modified grinding wheel designs to the three components of grinding force. The potential for facilitating force measurement with embedded strain sensors was evaluated for each of these designs.

- Significant levels of strain were predicted under applied axial loading, especially in areas of reduced wheel/disc thickness.
- Low levels of strain were predicted under applied tangential and normal loading, which were not consistently detectable at the SAW and MR sensor resolutions reported in the literature.

Therefore, it can be concluded that embedded strain sensors bear strong potential for axial force measurement in grinding wheels. Potential is limited for measurement of tangential or normal grinding forces, due to the low levels of strain which these generate. Novel strain sensors were deemed suitable for providing the resolution required to detect the level of strain typically exhibited by grinding wheels under axial loading, with Surface Acoustic Wave (SAW) sensors and Magnetostrictive (MR) sensors emerging as potential solutions here.

Future work to advance this study could focus on improvements to the beam bending and in-plane torsion test setups to reduce out-of-plane behaviour. Supports to stop beam or disc bending under applied shear or torsional loads could prevent the introduction of unexpected bending strains into the measurements, thereby improving measurement accuracy and enabling more accurate FE simulations.

Similarly, out-of-plane supports would be required to make the in-plane torsion testing setup a viable option for further project development. Future research could also investigate the optimal sensor orientations for normal strain measurement. The direction-dependant nature of strain means that strain sensors would have to be embedded in a suitable orientation relative to the wheel to properly capture the strain at a point, so this could be a key area for future investigations.

Finally, the potential of embedded sensors could be evaluated for locations other than on the grinding wheel. Locations such as the grinding wheel shaft may demonstrate more strain under applied tangential and normal loading, which may better facilitate their measurement with embedded strain sensors.

Bibliography

[1] H. ElMaraghy, L. Monostori, G. Schuh, and W. ElMaraghy, "Evolution and future of manufacturing systems," *CIRP Annals*, vol. 70, no. 2, pp. 635–658, Jan. 2021. DOI: 10.1016/j.cirp.2021.05.008.

[2] R. Teti, D. Mourtzis, D. M. D'Addona, and A. Caggiano, "Process monitoring of machining," *CIRP Annals*, vol. 71, no. 2, pp. 529–552, Jan. 2022. DOI: 10.1016/j.cirp.2022.05.009.

[3] J. Cao, E. Brinksmeier, M. Fu, *et al.*, "Manufacturing of advanced smart tooling for metal forming," *CIRP Annals*, vol. 68, no. 2, pp. 605–628, Jan. 2019. DOI: 10.1016/j.cirp.2019.05.001.

[4] J. Heidemann and R. Govindan, "Embedded sensor networks," in *Handbook of Networked and Embedded Control Systems*, D. Hristu-Varsakelis and W. S. Levine, Eds., MA, USA: Birkhäuser, 2005, pp. 721–738.

[5] R. Teti, K. Jemielniak, G. O'Donnell, and D. Dornfeld, "Advanced monitoring of machining operations," *CIRP Annals*, vol. 59, no. 2, pp. 717–739, Jan. 2010. DOI: 10.1016/j.cirp.2010.05.010.

[6] J. S. Chilles, A. Croxford, and I. P. Bond, "Design of an embedded sensor for improved structural performance," *Smart Materials and Structures*, vol. 24, no. 11, Art no. 115014, Oct. 2015. DOI: 10.1088/0964-1726/24/11/115014.

[7] V. Kalinin, "Wireless physical SAW sensors for automotive applications," in *IEEE International Ultrasonics Symposium*, FL, USA, Oct. 2011, pp. 212–221. DOI: 10.1109/ULTSYM.2011.0053.

[8] J. F. G. Oliveira, E. J. Silva, C. Guo, and F. Hashimoto, "Industrial challenges in grinding," *CIRP Annals*, vol. 58, no. 2, pp. 663–680, Jan. 2009. DOI: 10.1016/j.cirp.2009.09.006.

[9] B. Karpuschewski and I. Inasaki, "Monitoring systems for grinding processes," in *Condition Monitoring and Control for Intelligent Manufacturing*, L. Wang and R. X. Gao, Eds., London, England: Springer, 2006.

[10] F. Klocke, S. L. Soo, B. Karpuschewski, *et al.*, "Abrasive machining of advanced aerospace alloys and composites," *CIRP Annals*, vol. 64, no. 2, pp. 581–604, Jan. 2015. DOI: 10.1016/j.cirp.2015.05.004.

[11] N. Ceylan, S. Kacar, E. Guney, and C. Bayilmis, "Detection of grinding burn fault in bearings by squeeze net," in *30th Signal Processing and Communications Applications Conference*, Safranbolu, Turkey, May 2022, pp. 1–4. DOI: 10.1109/SIU55565.2022.9864895.

[12] E. Brazel, "Power and position-oriented process monitoring of freeform abrasive machining," Ph.D. Thesis, Deptartment of Mechanical and Manufacturing Enginering, Trinity College Dublin, Dublin, Ireland, 2013.

[13] B. Denkena, L. de Leon, A. Turger, and L. Behrens, "Prediction of contact conditions and theoretical roughness in manufacturing of complex implants by toric grinding tools," *International Journal of Machine Tools and Manufacture*, vol. 50, no. 7, pp. 630–636, Jul. 2010. DOI: 10.1016/j.ijmachtools.2010.03.008.

[14] C H Liu, C. C. A. Chen, C. Y. Lin, and C. J. Lin, "A Three-Component Strain Gage Dynamometer for Grinding and Polishing Force Measurement," *Journal of Materials Engineering and Performance*, vol. 14, pp. 173–178, Apr. 2005. DOI: 10.1361/10599490522374.

[15] G. K. Lal, "Forces in vertical surface grinding," *International Journal of Machine Tool Design and Research*, vol. 8, no. 1, pp. 33–43, Mar. 1968. DOI: 10.1016/0020-7357(68)90009-7.

[16] T. Onishi, Y. Murata, K. Fujiwara, M. Sakakura, and K. Ohashi, "Accurate estimation of workpiece dimension in plunge grinding without sizing gauge," *Precision Engineering*, vol. 74, pp. 441–446, Mar. 2022. DOI: 10.1016/j.precisioneng.2021.08.012.

[17] G. Q. Yin, Y. D. Gong, Y. W. Li, and J. Cheng, "Research on force and temperature characteristics of novel point grinding wheels," *Journal of Mechanical Science and Technology*, vol. 32, no. 8, pp. 3817–3834, Aug. 2018. DOI: 10.1007/s12206-018-0734-3.

[18] A. P. Walsh, B. Baliga, and P. D. Hodgson, "Force modelling of the crankshaft pin grinding process," *Proceedings of the Institution of Mechanical Engineers, Part D: Journal of Automobile Engineering*, vol. 218, no. 3, pp. 219–227, Mar. 2004. DOI: 10.1243/095440704322955768.

[19] P. Herzenstiel, R. C. Ching, S. Ricker, A. Menzel, P. Steinmann, and J. Aurich, "Interaction of process and machine during high-performance grinding: Towards a comprehensive simulation concept," *International Journal of Manufacturing Technology and Management*, vol. 12, no. 1-3, pp. 155–170, Jan. 2007. DOI: 10.1504/IJMTM.2007.014146.

[20] S. Mirzamohamadi, M. M. Sheikhi, M. R. Karafi, M. Ghodsi, and S. Ghorbanirezaei, "Novel contactless hybrid static magnetorestrictive force-torque (CHSMFT) sensor using galfenol," *Journal of Magnetism and Magnetic Materials*, vol. 553, Art no. 168969, Jul. 2022. DOI: 10.1016/j.jmmm.2021.168969.

[21] B. Lin, Y. Liu, Y. Cai, *et al.*, "A high Q value ScAlN/AlN-based SAW resonator for load sensing," in *IEEE Transactions on Electron Devices*, Conference Name: IEEE Transactions on Electron Devices, vol. 68, Oct. 2021, pp. 5192–5197. DOI: 10.1109/TED.2021.3107232.

[22] W. Zheng, B. Wang, H. Liu, X. Wang, Y. Li, and C. Zhang, "Bio-inspired magnetostrictive tactile sensor for surface material recognition," *IEEE Transactions on Magnetics*, vol. 55, no. 7, pp. 1–7, Jul. 2019. DOI: 10.1109/TMAG.2019.2898546.

[23] V. Kalinin, A. Leigh, A. Stopps, and S. B. Hanssen, "SAW torque sensor for marine applications," in *Joint Conference of the European Frequency and Time Forum and IEEE International Frequency Control Symposium*, Besancon, France, Jul. 2017, pp. 347–352. DOI: 10.1109/FCS.2017.8088889.

[24] M. Banther, Y. Huang, and W. Messner, "Optimal strain gauge placement for an instrumented disk drive suspension," in *Proceedings of the 1998 American Control Conference*, vol. 5, PA, USA, Jun. 1998, pp. 3023–3027. DOI: 10.1109/ACC.1998.688412.

[25] V. Lertchirakarn, J. Palamara, and H. H. Messer, "Finite element analysis and strain-gauge studies of vertical root fracture," *Journal of Endodontics*, vol. 29, no. 8, pp. 529–534, Aug. 2003. DOI: 10.1097/00004770-200308000-00009.

[26] B. Chen, X. Wu, and X. Peng, "Finite element analysis of ring strain sensor," *Sensors and Actuators*, vol. 139, no. 1, pp. 66–69, Sep. 2007. DOI: 10.1016/j.sna.2007.02.027.

[27] V. Kalinin, G. Bown, and A. Leigh, "P1K-3 contactless torque and temperature sensor based on SAW resonators," in *IEEE International Ultrasonics Symposium*, BC, Canada, Oct. 2006, pp. 1490–1493. DOI: 10.1109/ULTSYM.2006.374.

[28] T. Tomiyama, E. Lutters, R. Stark, and M. Abramovici, "Development capabilities for smart products," *CIRP Annals*, vol. 68, no. 2, pp. 727–750, Jan. 2019. DOI: 10.1016/j.cirp.2019.05.010.

[29] J. Lenz, E. MacDonald, R. Harik, and T. Wuest, "Optimizing smart manufacturing systems by extending the smart products paradigm to the beginning of life," *Journal of Manufacturing Systems*, vol. 57, pp. 274–286, Oct. 2020. DOI: 10.1016/j.jmsy.2020.10.001.

[30] A. Schütze, N. Helwig, and T. Schneider, "Sensors 4.0 – smart sensors and measurement technology enable Industry 4.0," *Journal of Sensors and Sensor Systems*, vol. 7, no. 1, pp. 359–371, May 2018. DOI: 10.5194/jsss-7-359-2018.

[31] Y. Hamed, G. O'Donnell, N. Lishchenko, and I. Munina, "Strain sensing technology to enable next-generation industry and smart machines for the factories of the future: A review," *IEEE Sensors Journal*, vol. 23, no. 1, pp. 618–649, Nov. 2023. DOI: 10.1109/JSEN.2023.3313013.

[32] M. Javaid, A. Haleem, R. P. Singh, S. Rab, and R. Suman, "Significance of sensors for industry 4.0: Roles, capabilities, and applications," *Sensors International*, vol. 2, Art no. 100110, Jan. 2021. DOI: 10.1016/j.sintl.2021.100110.

[33] J. Tlusty and G. C. Andrews, "A critical review of sensors for unmanned machining," *CIRP Annals*, vol. 32, no. 2, pp. 563–572, Jan. 1983. DOI: 10.1016/S0007-8506(07)60184-X.

[34] G. Byrne, D. Dornfield, I. Inasaki, G. Ketteler, W. Konig, and R. Teti, "Tool condition monitoring (TCM) — The status of research and industrial application," *CIRP Annals*, vol. 44, no. 2, pp. 541–567, Jan. 1995. DOI: 10.1016/S0007-8506(07)60503-4.

[35] M. Santochi and G. Dini, "Sensor technology in assembly systems," *CIRP Annals*, vol. 47, no. 2, pp. 503–524, Jan. 1998. DOI: 10.1016/S0007-8506(07)63239-9.

[36] G. O'Donnell, P. Young, K. Kelly, and G. Byrne, "Towards the improvement of tool condition monitoring systems in the manufacturing environment," *Journal of Materials Processing Technology*, vol. 119, no. 1, pp. 133–139, Dec. 2001. DOI: 10.1016/S0924-0136(01)00928-1.

[37] F. Bleicher, D. Biermann, W. G. Drossel, H. C. Moehring, and Y. Altintas, "Sensor and actuator integrated tooling systems," *CIRP Annals*, vol. 72, no. 2, pp. 673–696, Jan. 2023. DOI: 10.1016/j.cirp.2023.05.009.

[38] U. Thombansen, G. Buchholz, and D. Frank, "Design framework for model-based self-optimizing manufacturing systems," *International Journal of Advanced Manufacturing Technology*, vol. 97, pp. 519–528, Jul. 2018. DOI: 10.1007/s00170-018-1951-8.

[39] S. Addepalli, T. Weyde, B. Namoano, *et al.*, "Automation of knowledge extraction for degradation analysis," *CIRP Annals*, vol. 72, no. 1, pp. 33–36, Jan. 2023. DOI: 10.1016/j.cirp.2023.03.013.

[40] A. Svensson and K. Wennerstrom, "Predictive maintenance in production robots in a real world industrial setting," Master's Thesis, Department of Engineering, Chalmers University of Technology, Gothenburg, Sweden, 2023.

[41] D. Böttger, B. Stampfer, D. Gauder, *et al.*, "Concept for soft sensor structure for turning processes of AISI4140," *Technisches Messen*, vol. 87, no. 12, pp. 745–756, Dec. 2020. DOI: 10.1515/teme-2020-0054.

[42] D. Dornfield, Y. Lee, and A. Chang, "Monitoring of ultraprecision machining processes," *International Journal of Advanced Manufacturing Technology*, vol. 21, pp. 571–578, 2003. DOI: 10.1007/s00170-002-1294-.

[43] R. Teti and G. F. Micheletti, "Tool wear monitoring through acoustic emission," *CIRP Annals*, vol. 38, no. 1, pp. 99–102, Jan. 1989. DOI: 10.1016/S0007-8506(07)62660-2.

[44] B. Denkena, M. A. Dittrich, F. Uhlich, M. Wichmann, and M. Mücke, "Process parallel simulation of workpiece temperatures using sensory workpieces," *CIRP Journal of Manufacturing Science and Technology*, vol. 21, pp. 140–149, May 2018. DOI: 10.1016/j.cirpj.2018.01.004.

[45] W. Maier, H. C. Möhring, and K. Werkle, "Tools 4.0 – Intelligence starts on the cutting edge," in *Procedia Manufacturing*, vol. 24, 2018, pp. 299–304. DOI: 10.1016/j.promfg.2018.06.024.

[46] T. Junge, T. Mehner, A. Nestler, A. Schubert, and T. Lampke, "Metrological characterization of the thermomechanical influence of the cross-section of the undeformed chip on the surface properties in turning of the aluminum alloy EN AW-2017," *Technisches Messen*, vol. 87, no. 12, pp. 777–786, Nov. 2020. DOI: 10.1515/teme-2020-0059.

[47] R. Wegert, V. Guski, H. C. Möhring, and S. Schmauder, "Temperature monitoring in the subsurface during single lip deep hole drilling: Measuring of the thermomechanical load at different cutting parameters, including wear and simulative validation," *Technisches Messen*, vol. 87, no. 12, pp. 757–767, Dec. 2020. DOI: 10.1515/teme-2020-0055.

[48] A. Minora, L. Costa, D. Tolochenko, S. Kianoush, V. Rampa, and S. Savazzi, "Radar and infra-red array sensor fusion in a robotized environment: An experimental study," in *IEEE International Conference on Industrial Technology*, FL, USA, Apr. 2023, pp. 1–8. DOI: 10.1109/ICIT58465.2023.10143104.

[49] M. H. Rahimi, H. N. Huynh, and Y. Altintas, "On-line chatter detection in milling with hybrid machine learning and physics-based model," *CIRP Journal of Manufacturing Science and Technology*, vol. 35, pp. 25–40, Nov. 2021. DOI: 10.1016/j.cirpj.2021.05.006.

[50] M. Hassan, A. Sadek, and M. H. Attia, "Novel sensor-based tool wear monitoring approach for seamless implementation in high speed milling applications," *CIRP Annals*, vol. 70, no. 1, pp. 87–90, Jan. 2021. DOI: 10.1016/j.cirp.2021.03.024.

[51] D. Mandal and S. Banerjee, "Surface Acoustic Wave (SAW) Sensors: Physics, Materials, and Applications," *Sensors*, vol. 22, no. 3, p. 820, Jan. 2022. DOI: 10.3390/s22030820.

[52] H. K. Tönshoff, T. Friemuth, and J. C. Becker, "Process monitoring in grinding," *CIRP Annals*, vol. 51, no. 2, pp. 551–571, Jan. 2002. DOI: 10.1016/S0007-8506(07)61700-4.

[53] Y. Altintas, A. Verl, C. Brecher, L. Uriarte, and G. Pritschow, "Machine tool feed drives," *CIRP Annals*, vol. 60, no. 2, pp. 779–796, Jan. 2011. DOI: 10.1016/j.cirp.2011.05.010.

[54] K. Jemielniak, "Commercial tool condition monitoring systems," *International Journal of Advanced Manufacturing Technology*, vol. 15, pp. 711–721, Sep. 1999. DOI: 10.1007/s001700050123.

[55] X. Li and S. K. Tso, "Drill wear monitoring based on current signals," *Wear*, vol. 231, no. 2, pp. 172–178, Jul. 1999. DOI: 10.1016/S0043-1648(99)00130-1.

[56] T. Y. Kim, J. Woo, D. Shin, and J. Kim, "Indirect cutting force measurement in multi-axis simultaneous NC milling processes," *International Journal of Machine Tools and Manufacture*, vol. 39, no. 11, pp. 1717–1731, Nov. 1999. DOI: 10.1016/S0890-6955(99)00027-9.

[57] E. Brazel, R. Hanley, R. Cullinane, and G. O'Donnell, "Position-oriented process monitoring in freeform abrasive machining," *The International Journal of Advanced Manufacturing Technology*, vol. 69, no. 5, pp. 1443–1450, Nov. 2013. DOI: 10.1007/s00170-013-5111-x.

[58] R. Teti, I. S. Jawahir, K. Jemielniak, T. Segreto, S. Chen, and J. Kossakowska, "Chip Form Monitoring through Advanced Processing of Cutting Force Sensor Signals," *CIRP Annals*, vol. 55, no. 1, pp. 75–80, Jan. 2006. DOI: 10.1016/S0007-8506(07)60370-9.

[59] M. P. Groover, *Fundamentals of Modern Manufacturing- Materials, Processes, and Systems*, 7th ed. MA, USA: John Wiley & Sons Inc., 2019.

[60] B. Rowe, *Modern Grinding Technology and Systems*. Basel, Switzerland: MPDI, 2019.

[61] B. Rowe, *Principles of Modern Grinding Technology*, 2nd ed. Oxford, England: Elsevier, 2014.

[62] H. K. Tönshoff, B. Karpuschewski, T. Mandrysch, and I. Inasaki, "Grinding process achievements and their consequences on machine tools challenges and opportunities," *CIRP Annals*, vol. 47, no. 2, pp. 651–668, Jan. 1998. DOI: 10.1016/S0007-8506(07)63247-8.

[63] P. F. Ostwald and J. Munoz, *Manufacturing Processes and Systems*, 9th ed. NY, USA: John Wiley & Sons Inc., 1997.

[64] B. Denkena, T. Grove, and H. Lucas, "Influences of grinding with toric CBN grinding tools on surface and subsurface of 1.3344PM steel," *Journal of Materials Processing Technology*, vol. 229, pp. 541–548, Mar. 2016. DOI: 10.1016/j.jmatprotec.2015.09.039.

[65] W. B. Rowe and T. Jin, "Temperatures in high efficiency deep grinding (HEDG)," *CIRP Annals*, vol. 50, no. 1, pp. 205–208, Jan. 2001. DOI: 10.1016/S0007-8506(07)62105-2.

[66] J. Yoshioka, "Ultra-precision grinding technology for brittle materials: Application to surface and centreless grinding processes," in *Proceedings of the American Society of Mechanical Engineers*, USA, 1985, pp. 209–227.

[67] M. Zhou and W. Zheng, "A model for grinding forces prediction in ultrasonic vibration assisted grinding of SiCp/Al composites," *International Journal of Advanced Manufacturing Technology*, vol. 87, no. 9, pp. 3211–3224, Dec. 2016. DOI: 10.1007/s00170-016-8726-x.

[68] Y.-h. He, Q. Zhou, J.-j. Zhou, and X.-j. Lang, "Comprehensive modeling approach of axial ultrasonic vibration grinding force," *Journal of Central South University*, vol. 23, no. 3, pp. 562–569, Mar. 2016. DOI: 10.1007/s11771-016-3103-3.

[69] G. Sun, F. Shi, and Z. Ma, "Effects of axial ultrasonic vibration on grinding quality in peripheral grinding and end grinding of ULE," *International Journal of Advanced Manufacturing Technology*, no. 109, pp. 2285–2298, Jul. 2020. DOI: 10.1007/s00170-020-05761-5.

[70] G. Sun, L. Zhao, Z. Ma, and Q. Zhao, "Force prediction model considering material removal mechanism for axial ultrasonic vibration-assisted peripheral grinding of Zerodur," *The International Journal of Advanced Manufacturing Technology*, vol. 98, no. 9, pp. 2775–2789, Oct. 2018. DOI: 10.1007/s00170-018-2457-0.

[71] P. Durgumahanti, V. Singh, and P. Venkateswara Rao, "A new model for grinding force prediction and analysis," *International Journal of Machine Tools and Manufacture*, vol. 50, no. 3, pp. 231–240, Mar. 2010. DOI: 10.1016/j.ijmachtools.2009.12.004.

[72] S. Huang and X. Yu, "A study of grinding forces of SiCp/Al composites," *International Journal of Advanced Manufacturing Technology*, vol. 94, no. 9, pp. 3633–3639, Feb. 2018. DOI: 10.1007/s00170-017-1115-2.

[73] L. Lichun, F. Jizai, and J. Peklenik, "A study of grinding force mathematical model," *CIRP Annals*, vol. 29, no. 1, pp. 245–249, Jan. 1980. DOI: 10.1016/S0007-8506(07)61330-4.

[74] S. Lu, H. Gao, Y. Bao, and Q. Xu, "A model for force prediction in grinding holes of SiCp/Al composites," *International Journal of Mechanical Sciences*, vol. 160, pp. 1–14, Sep. 2019. DOI: 10.1016/j.ijmecsci.2019.06.025.

[75] H. S. Qi, W. B. Rowe, and B. Mills, "Contact length in grinding: Part 1: Contact length measurement," *Proceedings of the Institution of Mechanical Engineers, Part J: Journal of Engineering Tribology*, vol. 211, no. 1, pp. 67–76, Jan. 1997. DOI: 10.1243/1350650971542327.

[76] H. K. Tönshoff, M. Zinngrebe, and M. Kemmerling, "Optimization of Internal Grinding by Microcomputer-Based Force Control," *CIRP Annals*, vol. 35, no. 1, pp. 293–296, Jan. 1986. DOI: 10.1016/S0007-8506(07)61891-5.

[77] Y. Kita, M. Ido, and S. Hata, "The mechanism of metal removal by an abrasive tool," *Wear*, vol. 47, no. 1, pp. 185–193, Mar. 1978. DOI: 10.1016/0043-1648(78)90214-4.

[78] T. Bhowmick, N. Dhar, and J. Rana, "Development of a grinding dynamometer for an industrial model," in *Proceeding of the 4th International Conference on Mechanical Engineering*, Bangladesh, Dec. 2001.

[79] J. Zhang, B. Liu, M. Qian, X. Zhu, and R. Kang, "A novel piezoelectric grinding dynamometer for monitoring ultra-precision grinding of silicaon wafers," *Advanced*

Materials Research, vol. 126-128, pp. 707–712, 2010. DOI: 10.4028/www.scientific.net/AMR.126-128.707.

[80] I. Faridmehr, M. H. Osman, A. B. Adnan, A. F. Nejad, R. Hodjati, and M. Azimi, "Correlation between Engineering Stress-Strain and True Stress-Strain Curve," *American Journal of Civil Engineering and Architecture*, vol. 2, no. 1, pp. 53–59, DOI: 10.12691/ajcea-2-1-6.

[81] S. Timoshenko, *History of Strength of Materials*. MA, USA: Courier Corporation, 1983.

[82] P. A. Claisse, *Civil engineering Materials*. Oxford, England: Elsevier, 2016.

[83] B. S. Cook, R. Vyas, S. Kim, *et al.*, "RFID-based sensors for zero-power autonomous wireless sensor networks," *IEEE Sensors Journal*, vol. 14, no. 8, pp. 2419–2431, Aug. 2014. DOI: 10.1109/JSEN.2013.2297436.

[84] S. Soloman, *Sensors Handbook*, 2nd. IL, USA: McGraw Hill, 2010.

[85] V. Tsouti, V. Mitrakos, P. Broutas, and S. Chatzandroulis, "Modeling and development of a flexible carbon black-based capacitive strain sensor," *IEEE Sensors Journal*, vol. 16, no. 9, pp. 3059–3067, May 2016. DOI: 10.1109/JSEN.2016.2524508.

[86] H. Souri, H. Banerjee, A. Jusufi, *et al.*, "Wearable and stretchable strain sensors: Materials, sensing mechanisms, and applications," *Advanced Intelligent Systems*, vol. 2, no. 8, Art no. 2000039, 2020. DOI: 10.1002/aisy.202000039.

[87] J. Shieh, J. E. Huber, N. A. Fleck, and M. F. Ashby, "The selection of sensors," *Progress in Materials Science*, vol. 46, no. 3, pp. 461–504, Jan. 2001. DOI: 10.1016/S0079-6425(00)00011-6.

[88] J. Sirohi and I. Chopra, "Fundamental understanding of piezoelectric strain sensors," *Journal of Intelligent Material Systems and Structures*, vol. 11, no. 4, pp. 246–257, Apr. 2000. DOI: 10.1106/8BFB-GC8P-XQ47-YCQ0.

[89] K. Masláková, F. Trebuňa, P. Frankovský, and M. Binda, "Applications of the strain gauge for determination of residual stresses using ring-core method," *Procedia Engineering*, Modelling of Mechanical and Mechatronics Systems, vol. 48, pp. 396–401, Jan. 2012. DOI: 10.1016/j.proeng.2012.09.531.

[90] K. Hoffmann, *An Introduction to Measurements using Strain Gages*, Issue 3. Darmstadt, Germany: Hottinger Baldwin Messtechnik GmbH, Mar. 1987.

[91] K. Subrahmanya, K. Vadivuchezhian, and N. Chockappan, "Experimental verification of effect of adhesive layer thickness used for strain gauge mounting," *Advanced Materials Research*, vol. 1119, pp. 789–793, 2015. DOI: 10.4028/www.scientific.net/AMR.1119.789.

[92] E. Komurlu, F. Cihangir, A. Kesimal, and S. Demir, "Effect of adhesive type on the measurement of modulus of elasticity using electrical resistance strain gauges,"

Arabian Journal for Science and Engineering, vol. 41, no. 2, pp. 433–441, Feb. 2016. DOI: 10.1007/s13369-015-1837-0.

[93] J. McLoughlin, M. Munko, M. A. V. Camacho, F. Cuthill, and S. L. Dubon, "Use of digital image correlation and machine learning for the optimal strain placement in a full scale composite tidal turbine blade," in *Nineteenth International Conference on Condition Monitoring and Asset Management*, Northmpton, England, Sep. 2023. DOI: 10.1784/cm2023.2d4.

[94] K. Hoffmann, *Applying the Wheatstone Bridge circuit*. HBM, 2009. [Online]. Available: http://eln.teilam.gr/sites/default/files/Wheatstone%20bridge.pdf (visited on 02/05/2024).

[95] J. Goszczak, "Torque measurement issues," in *IOP Conference Series- Materials Science and Engineering*, vol. 148, Krakow, Poland, Sep. 2016, Art no. 012041. DOI: 10.1088/1757-899X/148/1/012041.

[96] S. Vanyeyev, D. Miroshnichenko, T. Rodymchenko, M. Protsenko, and D. Smolenko, "Data measuring system for torque measurement on running shafts based on a non-contact torsional dynamometer," *Journal of Engineering Sciences*, vol. 6, pp. 17–23, Jan. 2019. DOI: 10.21272/es.2019.6(2).e3.

[97] O. Engineering, *Biaxial 90° T Rosette Strain Gauges*. [Online]. Available: https://www.omega.co.uk/pptst/SGD_3-ELEMENT90.html (visited on 01/21/2024).

[98] O. Engineering, *60º Delta Rosette Strain Gauge*. [Online]. Available: https://www.omega.co.uk/pptst/SGD_3-ELEMENT60.html (visited on 01/21/2024).

[99] O. Engineering, *45º Strain Gauges, 3 Element Rosette*, en-in. [Online]. Available: https://in.omega.com/pptst/SGD_3-ELEMENT45.html (visited on 01/21/2024).

[100] L. Cai, L. Song, P. Luan, *et al.*, "Super-stretchable, transparent carbon nanotube-based capacitive strain sensors for human motion detection," *Scientific Reports*, vol. 3, no. 1, pp. 3048–3058, Oct. 2013. DOI: 10.1038/srep03048.

[101] T. Wu, G. Liu, S. Fu, and F. Xing, "Recent progress of fiber-optic sensors for the structural health monitoring of civil infrastructure," *Sensors*, vol. 20, no. 16, p. 4517, Jan. 2020. DOI: 10.3390/s20164517.

[102] S. J. Mihailov, "Fiber Bragg grating sensors for harsh environments," *Sensors*, vol. 12, no. 2, pp. 1898–1918, Feb. 2012. DOI: 10.3390/s120201898.

[103] S. M. M. Quintero, A. M. B. Braga, H. I. Weber, A. C. Bruno, and J. F. D. F. Araújo, "A Magnetostrictive Composite-Fiber Bragg Grating Sensor," *Sensors*, vol. 10, no. 9, pp. 8119–8128, Sep. 2010. DOI: 10.3390/s100908119.

[104] J. Albert, L. Y. Shao, and C. Caucheteur, "Tilted fiber Bragg grating sensors," *Laser & Photonics Reviews*, vol. 7, no. 1, pp. 83–108, 2013. DOI: 10.1002/lpor.201100039.

[105] I. Floris, J. M. Adam, P. A. Calderón, and S. Sales, "Fiber optic shape sensors: A comprehensive review," *Optics and Lasers in Engineering*, vol. 139, Art no. 106508, Apr. 2021. DOI: 10.1016/j.optlaseng.2020.106508.

[106] E. Hristoforou and A. Ktena, "Magnetostriction and magnetostrictive materials for sensing applications," Proceedings of the Joint European Magnetic Symposia, vol. 316, no. 2, pp. 372–378, Sep. 2007. DOI: 10.1016/j.jmmm.2007.03.025.

[107] A. Tavassolizadeh, K. Rott, T. Meier, *et al.*, "Tunnel magnetoresistance sensors with magnetostrictive electrodes: Strain sensors," *Sensors*, vol. 16, no. 11, p. 1902, Nov. 2016. DOI: 10.3390/s16111902.

[108] H. Kwun and K. A. Bartels, "Magnetostrictive sensor technology and its applications," *Ultrasonics*, vol. 36, no. 1, pp. 171–178, Feb. 1998. DOI: 10.1016/S0041-624X(97)00043-7.

[109] T. Calkins, A. Flatau, and M. Dapino, "Overview of magnetostrictive sensor technology," *Journal of Intelligent Material Systems and Structures*, vol. 18, pp. 1057–1066, Oct. 2007. DOI: 10.1177/1045389X06072358.

[110] M. Löhndorf, S. Dokupil, M. .-. Bootsmann, *et al.*, "Characterization of magnetostrictive TMR pressure sensors by MOKE," *Journal of Magnetism and Magnetic Materials*, vol. 316, no. 2, pp. 223–225, Sep. 2007. DOI: 10.1016/j.jmmm.2007.02.095.

[111] L. Ren, K. Yu, and Y. Tan, "Applications and advances of magnetoelastic sensors in biomedical engineering: A review," *Materials*, vol. 12, no. 7, p. 1135, Apr. 2019. DOI: 10.3390/ma12071135.

[112] R. Gonçalves, A. Larrea, T. Zheng, *et al.*, "Synthesis of highly magnetostrictive nanostructures and their application in a polymer-based magnetoelectric sensing device," *European Polymer Journal*, vol. 84, pp. 685–692, 2016. DOI: 10.1016/j.eurpolymj.2016.09.055.

[113] K. Liang, S. Angelopoulos, G. Lepipas, *et al.*, "Sensor to monitor localised stresses on steel surfaces using the magnetostrictive delay line technique," *Sensors*, vol. 19, no. 21, pp. 4797–4805, Jan. 2019. DOI: 10.3390/s19214797.

[114] G. Zhang, "Nanostructure-enhanced surface acoustic waves biosensor and its computational modeling," *Journal of Sensors*, vol. 2009, no. 2, pp. 1–11, Jan. 2009. DOI: 10.1155/2009/215085.

[115] A. Namdeo and H. Nemade, "Simulation on effects of electrical loading due to interdigital transducers in surface acoustic wave resonators," *Procedia Engineering*, vol. 64, pp. 322–330, Dec. 2013. DOI: 10.1016/j.proeng.2013.09.104.

[116] L. Reindl, G. Scholl, T. Ostertag, H. Scherr, U. Wolff, and F. Schmidt, "Theory and application of passive SAW radio transponders as sensors," *IEEE Transactions on Ultrasonics, Ferroelectrics, and Frequency Control*, vol. 45, no. 5, pp. 1281–1292, Sep. 1998. DOI: 10.1109/58.726455.

[117] L. Kelly, C. Chen, X. Bao, and P. Berini, "High-resolution surface acoustic wave (SAW) strain sensor based on acoustic Fabry-Pérot resonance," *Sensors and Actuators A: Physical*, vol. 338, p. 113 504, May 2022. DOI: 10.1016/j.sna.2022.113504.

[118] X. Tan, Z. Zhou, L. Zhang, *et al.*, "A passive wireless triboelectric sensor via a surface acoustic wave resonator (SAWR)," *Nano Energy*, vol. 78, Art no. 105307, Dec. 2020. DOI: 10.1016/j.nanoen.2020.105307.

[119] A. Binder, R. Fachberger, E. Kaldjob, and B. Geck, "Packaging and antenna design for wireless SAW temperature sensors in metallic environments," *IEEE Sensors Journal*, vol. 2009 IEEE, pp. 807–810, Oct. 2009. DOI: 10.1109/ICSENS.2009.5398549.

[120] K. Tan, Z. Ji, J. Zhou, *et al.*, "Machine learning empowered thin film acoustic wave sensing," *Applied Physics Letters*, vol. 122, no. 1, Art no. 014101, Jan. 2023. DOI: 10.1063/5.0131779.

[121] R. Stoney, B. Donohoe, D. Geraghty, and G. O'Donnell, "The development of surface acoustic wave sensors (SAWs) for process monitoring," in *Procedia CIRP*, vol. 1, Jan. 2012, pp. 569–574. DOI: 10.1016/j.procir.2012.05.001.

[122] B. Donohoe, D. Geraghty, and G. O'Donnell, "Wireless calibration of a surface acoustic wave resonator as a strain sensor," *IEEE Sensors Journal*, vol. 11, no. 4, pp. 1026–1032, Apr. 2011. DOI: 10.1109/JSEN.2010.2070492.

[123] W. Zhou, H. Su, J. Dai, T. Yu, and Y. Zheng, "Numerical investigation on the influence of cutting-edge radius and grinding wheel speed on chip formation in SiC grinding," *Ceramics International*, vol. 44, no. 17, pp. 451–460, Dec. 2018. DOI: 10.1016/j.ceramint.2018.08.206.

[124] L. Li, Y. Zhang, X. Cui, *et al.*, "Mechanical behavior and modeling of grinding force: A comparative analysis," *Journal of Manufacturing Processes*, vol. 102, pp. 921–954, Sep. 2023. DOI: 10.1016/j.jmapro.2023.07.074.

[125] A. E. Tekkaya, K. Pöhlandt, and K. Lange, "Determining stress-strain curves of sheet metal in the plane torsion test," *CIRP Annals*, vol. 31, no. 1, pp. 171–174, Jan. 1982. DOI: 10.1016/S0007-8506(07)63291-0.

[126] Q. Yin, C. Soyarslan, K. Isik, and A. Tekkaya, "A grooved in-plane torsion test for the investigation of shear fracture in sheet materials," *International Journal of Solids and Structures*, vol. 66, pp. 121–132, Apr. 2015. DOI: 10.1016/j.ijsolstr.2015.03.032.

[127] A. Brosius, Q. Yin, A. Güner, and A. Tekkaya, "A new shear test for sheet metal characterization," *Steel Research International*, vol. 82, no. 4, pp. 323–328, 2011. DOI: 10.1002/srin.201000163.

[128] A. Logg, "Automating the finite element method," *Archives of Computational Methods in Engineering*, vol. 14, no. 2, pp. 93–138, Jun. 2007. DOI: 10.1007/s11831-007-9003-9.

[129] P. J. Kim, D. G. Lee, and J. K. Choi, "Grinding Characteristics of Carbon Fiber Epoxy Composite Hollow Shafts," *Journal of Composite Materials*, vol. 34, no. 23, pp. 2016–2035, Dec. 2000. DOI: 10.1177/002199800772661958.

[130] W. J. Liu, Z. J. Pei, and X. J. Xin, "Finite element analysis for grinding and lapping of wire-sawn silicon wafers," *Journal of Materials Processing Technology*, vol. 129, no. 1, pp. 2–9, Oct. 2002. DOI: 10.1016/S0924-0136(02)00565-4. (visited on 04/03/2024).

[131] G. Warnecke and C. Barth, "Optimization of the Dynamic Behavior of Grinding Wheels for Grinding of Hard and Brittle Materials Using the Finite Element Method," *CIRP Annals*, vol. 48, no. 1, pp. 261–264, Jan. 1999. DOI: 10.1016/S0007-8506(07)63179-5.

[132] A. Belhocine, "FE prediction of thermal performance and stresses in an automotive disc brake system," *International Journal of Advanced Manufacturing Technology*, vol. 89, pp. 3563–3578, Aug. 2016. DOI: 10.1007/s00170-016-9357-y.

[133] P. Grzes and M. Kuciej, "Coupled thermomechanical FE model of a railway disc brake for friction material wear calculations," *Wear*, vol. 530, Art no. 205049, Jul. 2023. DOI: https://doi.org/10.1016/j.wear.2023.205049.

[134] H. Lee, "Finite element analysis of a buried pipeline," MAI Thesis, Department of Engineering and Physical Science, University of Manchester, Manchester, England, 2010.

[135] S. Kock, G. Jacobs, D. Bosse, and F. Strangfeld, "Simulation Method for the Characterisation of the Torque Transducers in MN·m range," in *Journal of Physics: Conference Series*, vol. 1065, Aug. 2018, Art no. 042014. DOI: 10.1088/1742-6596/1065/4/042014.

[136] K. Kataoka, O. Doi, and M. Sato, "Residual Stress Measurement of Laminated Anisotropic Plate by Strain Gauge Method in Consideration of Strain Gauge Stiffness and Gauge Base Thickness," *Bulletin of JSME*, vol. 29, no. 248, pp. 393–399, 1986. DOI: 10.1299/jsme1958.29.393.

[137] J. Case, L. Chilver, and C. Ross, *Strength of Materials and Structures*, 4th ed. London, England: Arnold, 1999.

[138] C. Grant, "Mechanical testing and modelling of a bone-implant construct," Ph.D. Thesis, Science and Engineering Department, Queensland University of Technology, Brisbane, Australia, 2012.

[139] Transense, *Torque Measurement in Robotics Applications*. [Online]. Available: https://www.transense.com/saw-sense/torque-measurement-in-robotics-applications (visited on 04/06/2024).

A1 Experimental Setups

A1.1 Coordinate System Definition

A uniform coordinate system was used for all torsion tests conducted throughout the project, as is illustrated in Figure A1.1. The disc was aligned parallel to the Instron base (i.e. along the YZ plane), with the centre of its bottom surface defined as the origin. Rotation angles about the X axis were defined by the term α here. Counterclockwise rotations are associated with positive α values in this framework. Torsion was always applied about the vertical (X) axis in a clockwise direction, (i.e. negative α). The coordinate system was defined relative to the strain gauge positions for each experiment- strain gauges were located at $\alpha = 270°$ for all tests. The axial, tangential and normal forces acting on the wheel (F_a, F_t and F_n) were also defined in terms of this coordinate system- these were aligned with the X, Y and Z axes, respectively.

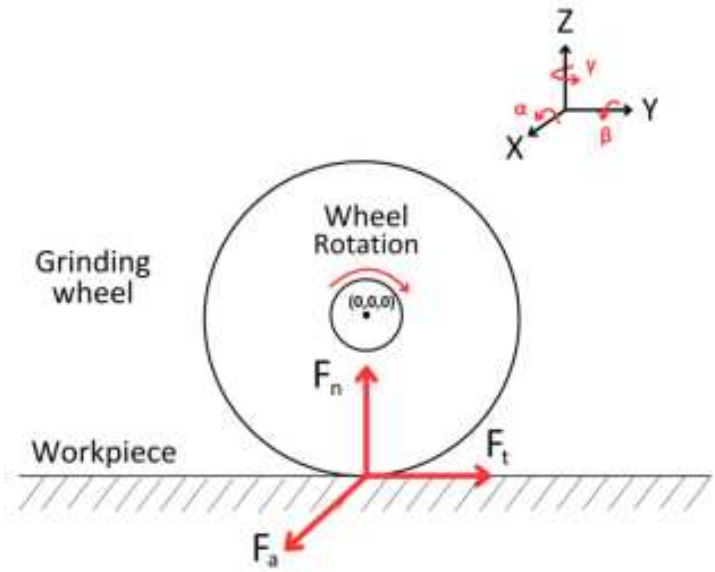

Figure A1.1: Disc coordinate system.

Reference axes were etched onto the disc surface to facilitate precise placement of strain gauges. Each strain gauge position was delineated in terms of its X, Y, and Z coordinates, as well as its angular orientation about the X axis, α. When clamps were attached to the disc during testing, their positions were similarly defined with X, Y, and Z coordinates. The angle between the clamp and strain gauge positions about the Y axis was denoted by ϕ. This approach is detailed in Figure A1.2.

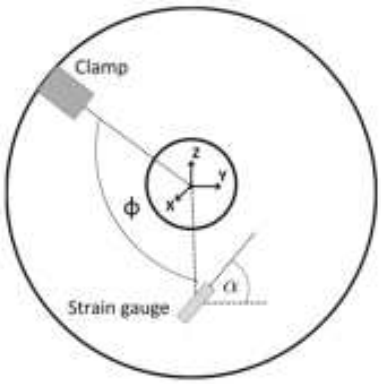

Figure A1.2: Strain gauge and clamp angle definitions.

A1.2 Experimental Coordinates

Component	Type	Manufacturer	Coordinates (mm)	Orientation
SG 1	Single gauge	Techni Measure	(63, 5, 4)	$\alpha = 134°$
SG 2	Single gauge	Techni Measure	(56, 5, 1)	$\alpha = 45°$
SG 3	Single gauge	Techni Measure	(43, 5, -1)	$\alpha = 47°$
SG 4	Single gauge	Techni Measure	(32, 5, 3)	$\phi = 45°$
Clamp 1	N/A	N/A	(-57, 0, -57)	$\phi = 45°$
Clamp 2	N/A	N/A	(90, 0, 0)	$\phi = 180°$
Clamp 3	N/A	N/A	(57, 0, -57)	$\phi = 315°$

Table A1.1: Coordinates for 5 mm disc experimental setup (Section 4.1.1).

Component	Type	Manufacturer	Coordinates (mm)	Orientation
SG 1	Rosette	Micro Measurements	(-55, 3, -7)	$\alpha = 51°$
SG 2	Rosette	Micro Measurements	(-53, 3, -1)	$\alpha = 96°$
SG 3	Rosette	Micro Measurements	(-51, 3, 4)	$\alpha = 141°$
Clamp	N/A	N/A	(-56, 0 , -56)	$\phi = 45°$

Table A1.2: Coordinates for first 3 mm disc experiment (Section 4.2.1.

The clamp coordinates given in each of the tables here represent the centre point of the contact area between clamp and disc bottom surface. Contact also occurs at the same points on the top surfaces, which was accounted for in the FE models.

Component	Type	Manufacturer	Coordinates (mm)	Orientation
SG 1	Rosette	Micro Measurements	(-55, 3, -7)	$\alpha = 51°$
SG 2	Rosette	Micro Measurements	(-53, 3, -1)	$\alpha = 96°$
SG 3	Rosette	Micro Measurements	(-51, 3, 4)	$\alpha = 141°$
Clamp Position 1	N/A	N/A	(-69, 0, -40)	$\phi = 30°$
Clamp Position 2	N/A	N/A	(-40, 0, -71)	$\phi = 60°$
Clamp Position 3	N/A	N/A	(0, 0, -88)	$\phi = 90°$
Clamp Position 4	N/A	N/A	(40, 0, -68)	$\phi = 120°$
Clamp Position 5	N/A	N/A	(-37, 0, -68)	$\phi = 240°$

Table A1.3: Coordinates for second 3 mm disc experiment (Section 4.3).

Component	Type	Manufacturer	Coordinates (mm)	Orientation
SG 1	Rosette	Micro Measurements	(2, 4, 269)	$\alpha = 135°$
SG 2	Rosette	Micro Measurements	(-1, 4, 269)	$\alpha = 0°$
SG 3	Rosette	Micro Measurements	(-5, 4, 305)	$\alpha = 45°$
SG 4	Tee	Micro Measurements	(-1, 4, 305)	$\alpha = 90°$
SG 5	Tee	Micro Measurements	(-5, 4, 305)	$\alpha = 0°$

Table A1.4: Coordinates for beam experiments (Sections 5.3.1 and 5.4).

A2 Additional FE Model Information

A2.1 Material Properties

Table A2.1 gives the relevant properties for the two materials applied in simulations in this project- AISI 1010 carbon steel and AISI 1340 carbon steel.

ASTM Designation	Elastic Modulus (GPa)	Shear Modulus (GPa)	Poisson's Ratio
AISI 1010 carbon steel	2.000×10^{11}	7.692×10^{10}	0.30
AISI 1340 carbon steel	2.074×10^{11}	8.039×10^{10}	0.29

Table A2.1: Material properties as per ANSYS Mechanical Library.

A2.2 Chapter 6 Meshing

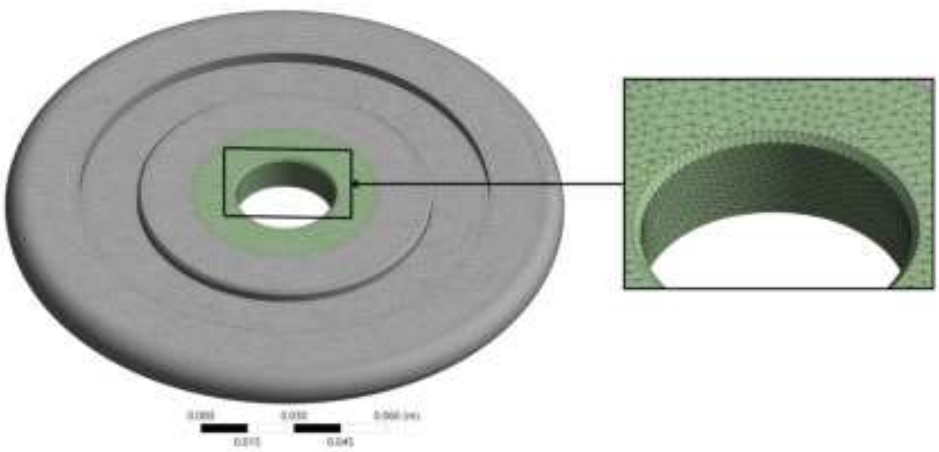

Figure A2.1: Grinding wheel mesh.

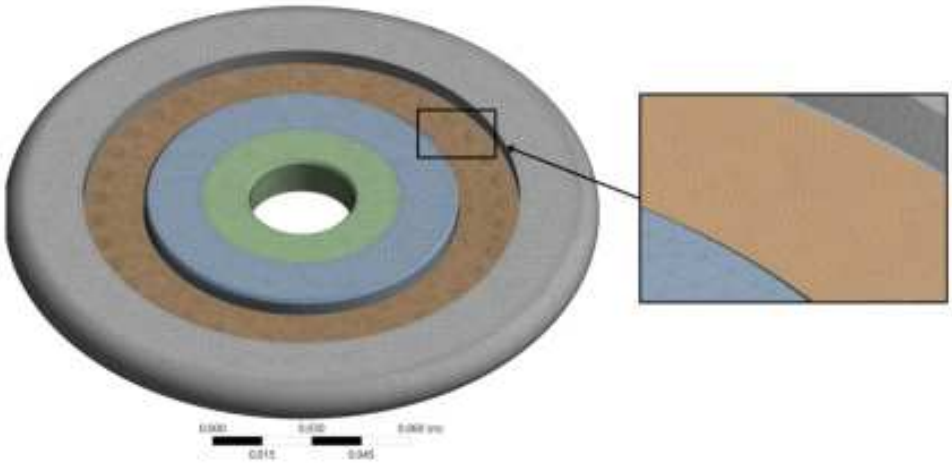

Figure A2.2: Thinned grinding wheel mesh.

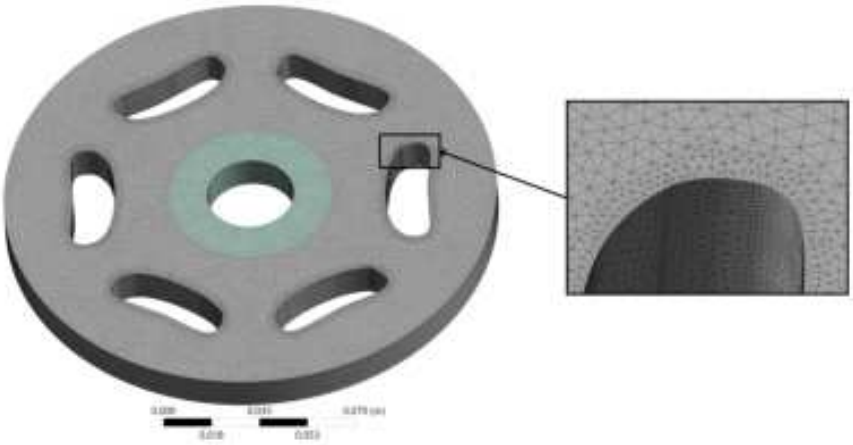

Figure A2.3: Slotted disc mesh.

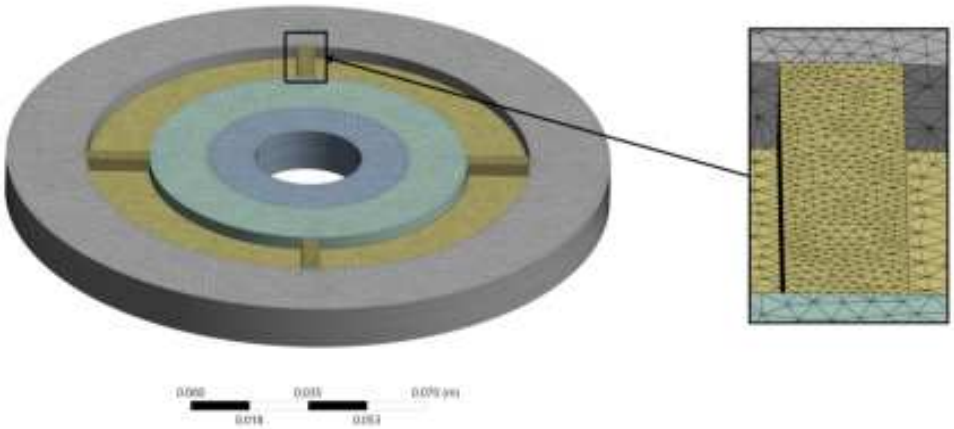

Figure A2.4: Bridge disc mesh.

A2.3 Chapter 6 Setup

Component	Coordinates (mm)	Orientation
Construction path (start)	(0, 6.5, 0)	N/A
Construction path (end)	(-90, 6.5, 0)	N/A
Applied remote force	(-63.4, 6.5, -63.4)	$\alpha = 45°$

Table A2.2: Construction path coordinates for grinding wheel simulations.